Multiwavelength campaign observations of a young solar-type star, EK Draconis. II. understanding prominence eruption through data-driven modeling and observed magnetic environment

Namekata, K.; Ikuta, K.; Petit, P.; Airapetian, V.S.; Vidotto, A.; Heinzel, P.; ... ; Shibata, K.

The Astrophysical Journal, 976:255 (19pp), 2024 December 1 https://doi.org/10.3847/1538-4357/ad85df

Multiwavelength Campaign Observations of a Young Solar-type Star, EK Draconis. II. Understanding Prominence Eruption through Data-driven Modeling and Observed Magnetic Environment

Kosuke Namekata[1,2,3,4,5], Kai Ikuta[6], Pascal Petit[7], Vladimir S. Airapetian[4,8], Aline A. Vidotto[9], Petr Heinzel[10,11], Jiří Wollmann[11], Hiroyuki Maehara[12], Yuta Notsu[13,14], Shun Inoue[2], Stephen Marsden[15], Julien Morin[16], Sandra V. Jeffers[17], Coralie Neiner[18], Rishi R. Paudel[19,20], Antoaneta A. Avramova-Boncheva[21], Keith Gendreau[20], and Kazunari Shibata[22,23]

[1] The Hakubi Center for Advanced Research, Kyoto University, Yoshida-Honmachi, Sakyo-ku, Kyoto 606-8501, Japan; namekata@kusastro.kyoto-u.ac.jp
[2] Department of Physics, Kyoto University, Kitashirakawa-Oiwake-cho, Sakyo-ku, Kyoto, 606-8502, Japan
[3] Heliophysics Science Division, NASA Goddard Space Flight Center, 8800 Greenbelt Road, Greenbelt, MD 20771, USA
[4] Department of Physics, American University, 4400 Massachusetts Ave NW, Washington, DC 20016, USA
[5] Division of Science, National Astronomical Observatory of Japan, NINS, Osawa, Mitaka, Tokyo, 181-8588, Japan
[6] Department of Multidisciplinary Sciences, The University of Tokyo, 3-8-1 Komaba, Meguro, Tokyo 153-8902, Japan
[7] Institut de Recherche en Astrophysique et Planétologie, Université de Toulouse, CNRS, CNES, 14 avenue Édouard Belin, 31400 Toulouse, France
[8] Sellers Exoplanetary Environments Collaboration, NASA Goddard Space Flight Center, Greenbelt, MD, USA
[9] Leiden Observatory, Leiden University, P.O. Box 9513, 2300 RA Leiden, The Netherlands
[10] Center of Excellence "Solar and Stellar Activity," University of Wrocław, Kopernika 11, PL-51622 Wrocław, Poland
[11] Astronomical Institute of Czech Academy of Sciences Fričova 298, 251 65, Ondřejov, Czech Republic
[12] Okayama Branch Office, Subaru Telescope, National Astronomical Observatory of Japan, NINS, Kamogata, Asakuchi, Okayama 719-0232, Japan
[13] Laboratory for Atmospheric and Space Physics, University of Colorado Boulder, 3665 Discovery Drive, Boulder, CO 80303, USA
[14] National Solar Observatory, 3665 Discovery Drive, Boulder, CO 80303, USA
[15] Centre for Astrophysics, University of Southern Queensland, Toowoomba, Queensland 4350, Australia
[16] LUPM, Université de Montpellier, CNRS, Place Eugène Bataillon, F-34095 Montpellier, France
[17] Max Planck Institute for Solar System Research, Justus-von-Liebig-weg 3, 37077 Göttingen, Germany
[18] LESIA, Paris Observatory, PSL University, CNRS, Sorbonne University, Université Paris Cité, 5 place Jules Janssen, 92195 Meudon, France
[19] University of Maryland, Baltimore County, 1000 Hilltop Circle, Baltimore, MD 21250, USA
[20] NASA Goddard Space Flight Center, Greenbelt, MD, USA
[21] The Institute of Astronomy and National Astronomical Observatory, Bulgarian Academy of Sciences, 72 Tsarigradsko Chaussee Blvd., 1784 Sofia, Bulgaria
[22] Kwasan Observatory, Kyoto University, Yamashina, Kyoto 607-8471, Japan
[23] School of Science and Engineering, Doshisha University, Kyotanabe, Kyoto 610-0321, Japan
Received 2024 August 3; revised 2024 October 4; accepted 2024 October 7; published 2024 November 27

Abstract

EK Draconis, a nearby young solar-type star (G1.5V, 50–120 Myr), is known as one of the best proxies for inferring the environmental conditions of the young Sun. The star frequently produces superflares, and Paper I presented the first evidence of an associated gigantic prominence eruption observed as a blueshifted Hα Balmer line emission. In this paper, we present the results of the dynamical modeling of the stellar eruption and examine its relationship to the surface starspots and large-scale magnetic fields observed concurrently with the event. By performing a 1D freefall dynamical model and a 1D hydrodynamic simulation of the flow along the expanding magnetic loop, we found that the prominence eruption likely occurred near the stellar limb (12^{+5}_{-5}-16^{+7}_{-7} degrees from the limb) and was ejected at an angle of 15^{+6}_{-5}-24^{+6}_{-6} degrees relative to the line of sight, and the magnetic structures can expand into a coronal mass ejection. The observed prominence displayed a terminal velocity of $\sim$0 km s^{-1} prior to disappearance, complicating the interpretation of its dynamics in Paper I. The models in this paper suggest that prominence's Hα intensity diminishes at around or before its expected maximum height, explaining the puzzling time evolution in observations. The Transiting Exoplanet Survey Satellite light curve modeling and (Zeeman) Doppler Imaging revealed large midlatitude spots with polarity inversion lines and one polar spot with dominant single polarity, all near the stellar limb during the eruption. This suggests that midlatitude spots could be the source of the gigantic prominence we reported in Paper I. These results provide valuable insights into the dynamic processes that likely influenced the environments of early Earth, Mars, Venus, and young exoplanets.

Unified Astronomy Thesaurus concepts: Stellar flares (1603); Stellar coronal mass ejections (1881); Optical flares (1166); Stellar x-ray flares (1637); Flare stars (540); G dwarf stars (556); Solar analogs (1941); Doppler imaging (400); Zeeman-Doppler imaging (1837); Starspots (1572)

1. Introduction

Solar and stellar flares are among the most powerful phenomena in the atmospheres of cool stars, observed across a wide range of wavelengths from radio to X-ray bands (K. Shibata & T. Magara 2011; A. O. Benz 2017). These flares result from the conversion of magnetic energy into kinetic and thermal energy via magnetic reconnection. The most powerful solar flares have energies around 10^{32} erg (A. G. Emslie et al. 2012), while cosmogenic radionuclide studies (F. Miyake et al. 2019; I. G. Usoskin 2023) and observations of Sun-like stars (H. Maehara et al. 2012; T. Shibayama et al. 2013; Y. Notsu et al. 2019; S. Okamoto et al. 2021) suggest potential

"superflares" ($>10^{33}$ erg) on our Sun. On the Sun, large flares often accompany coronal mass ejections (CMEs), which eject massive amounts of coronal material into space at high speeds, impacting planetary magnetospheres and ionospheres (e.g., M. Temmer 2021). Consequently, massive flares are garnering attention in terms of significant potential impacts on human society (e.g., E. W. Cliver et al. 2022).

Motivated by the recent successful detections of large numbers of exoplanets, there has been an increased focus on the space weather environments of other stellar systems (e.g., J. Linsky 2019). Numerous attempts have been made to estimate the complete X-ray and ultraviolet radiation (e.g., J. L. Linsky et al. 2014; C. P. Johnstone et al. 2019; K. Namekata et al. 2023) and plasma environments (e.g., B. E. Wood et al. 2005) around stars; however, characterizing these environments is often challenging because stars cannot be spatially resolved and the signals of astrospheres are too weak. Particularly, stellar CMEs associated with transient stellar flares present significant difficulties in the detection and characterization of their propagation (see reviews by R. A. Osten & S. J. Wolk 2017; M. Leitzinger & P. Odert 2022; K. Namekata et al. 2022a). Historically, observations of solar flares have guided both direct and indirect attempts to detect stellar CMEs. For example, numerous blueshifted emission profiles in chromospheric lines have been observed during flares from M/K dwarfs and active close binaries, which are interpreted as a signature of stellar prominence eruptions, the lower parts, or even cores of CMEs (E. R. Houdebine et al. 1990; E. L. E. Eason et al. 1992; A. G. Gunn et al. 1994; I. Crespo-Chacón et al. 2006; B. Fuhrmeister et al. 2008, 2011, 2018; K. Vida et al. 2016, 2019; M. Flores Soriano & K. G. Strassmeier 2017; S. Honda et al. 2018; P. Muheki et al. 2020a, 2020b; F. Koller et al. 2021; H. Maehara et al. 2021; S. Inoue et al. 2023, 2024; Y. Notsu et al. 2024). Though velocities are often low, some are fast enough to suggest prominence eruptions leading to CMEs (E. R. Houdebine et al. 1990; K. Vida et al. 2016, 2019; S. Inoue et al. 2023). Additionally, postflare coronal dimming (A. M. Veronig et al. 2021; R. O. P. Loyd et al. 2022) and type IV radio bursts (A. Zic et al. 2020; A. Mohan et al. 2024) have been reported to infer the occurrence of stellar CMEs mainly from M/K dwarfs. Current reports lack crucial details, such as type II radio bursts (M. K. Crosley & R. A. Osten 2018a, 2018b; J. Villadsen & G. Hallinan 2019), which indicate CME-driven shock formation and propagation. Therefore, the consensus in the stellar community is that direct evidence of stellar CME occurrence has not yet been reported. Numerical simulations assuming large-scale dipole magnetic fields suggest that a strong overlying coronal magnetic field may suppress eruptions (J. D. Alvarado-Gómez et al. 2018), indicating that stellar CMEs can be rare or their signal is too weak compared to the solar case. Comparing observations and theoretical models is important to reveal whether and how stellar eruptions happen, yet there is a notable lack of simultaneous data sets of stellar CME signatures and magnetic field mappings, and consequently, the connection between theoretical predictions and observational data remains suboptimal.

Previous attempts to detect stellar CMEs have been biased toward relatively cooler stars (e.g., M dwarfs), with minimal research conducted on solar-type stars (G-type main-sequence stars). However, observing solar-type stars is crucial as it provides a significant window into the past and future evolution of the Sun and solar system planets (M. Güdel et al. 1997; M. Güdel 2007). Previous observations of young solar-type stars suggest that the young Sun was highly active, possessed large surface magnetic flux (A. A. Vidotto et al. 2014; C. P. Folsom et al. 2016, 2018; O. Kochukhov et al. 2020), and frequently emitted superflares (M. Audard et al. 1999, 2000; S. Colombo et al. 2022; K. Namekata et al. 2022b; M. Yamashita et al. 2022). It is proposed that if these superflares are frequently associated with massive CMEs, the high-energy particles from these CMEs could have significantly altered the chemical composition of planets, potentially generating greenhouse gases, prebiotic chemistry, and complex biological molecules. (V. S. Airapetian et al. 2016; K. Kobayashi et al. 2023). In addition, the eruptive events could play a significant role in stellar mass and angular momentum loss evolution, which influences estimates of how active the Sun and stars were during their youth (e.g., R. A. Osten & S. J. Wolk 2015; S. R. Cranmer 2017; B. E. Wood et al. 2021). Therefore, investigating the occurrence of CMEs from young solar-type stars is an essential task that relates to fundamental questions about our origins.

With the aim of investigating signals of superflares and filament/prominence eruptions as indirect evidence of CMEs, we have conducted long-term spectroscopic monitoring observations of a young solar-type star, EK Draconis (EK Dra, HD 129333). EK Dra is a G1.5V dwarf with an age of 50–125 Myr, the effective temperature of 5560–5700 K, radius of 0.94 $R_\odot$, and mass of 0.95 $M_\odot$ (I. A. Waite et al. 2017; H. V. Şenavcıet al. 2021). It is a rapidly rotating star with a rotation period of ∼2.77 days (M. Audard et al. 1999; T. R. Ayres 2015; K. Namekata et al. 2022c), and it exhibits a high level of magnetic activity in the form of a hot and dense corona (e.g., L. Scelsi et al. 2005; J. L. Linsky et al. 2012; K. Namekata et al. 2023), strong surface magnetic field and large starspots (e.g., S. V. Berdyugina & S. P. Järvinen 2005; I. A. Waite et al. 2017; S. P. Järvinen et al. 2018) and frequent superflares (e.g., M. Audard et al. 1999, 2000; T. R. Ayres 2015; K. Namekata et al. 2022b, 2022c). These characteristics make this star one of the best targets to detect superflares and associated CMEs from an infant Sun at the time of the Hadean period on Earth.

As a result of our long-term monitoring observations since 2020, we have successfully detected the Hα line spectra of five superflares on EK Dra (K. Namekata et al. 2022b, 2022c, 2024). Among these, one event exhibited a blueshifted absorption component (K. Namekata et al. 2022c; later, followed up by M. Leitzinger et al. 2024), and two were accompanied by blueshifted emission components (K. Namekata et al. 2024, hereafter referred to as Paper I). Comparative analysis with solar observations suggests that the absorption profiles indicate filament eruptions occurring in front of the stellar disk, while the emission profiles imply prominence eruptions outside the stellar disk. Also, their high line-of-sight (LOS) velocities of 330–690 km s^{-1}, close to the escape velocity of ∼670 km s^{-1}, suggest the possible occurrence of stellar CMEs. This suggestion is supported by a recent 1D hydrodynamic (HD) simulation of the plasma flow along an expanding magnetic loop for the filament eruption (K. Ikuta & K. Shibata 2024). This discovery provides indirect evidence of stellar CMEs, marking the first indications specifically for young solar-type stars.

Among these discoveries, the massive prominence eruption on 2022 April 10 (labeled "E1" in Paper I) presents particularly intriguing and well-characterized observational properties. This event shows a very massive eruptive prominence with a mass of $\sim10^{20}$ g and possible X-ray coronal

dimming occurrence, providing the first multiwavelength characterization of stellar CME signatures. One of the intriguing aspects of this event is that the velocity of the eruption began near the escape speed at 690 km s^{-1}, decelerated approximately along with surface gravity, and showed a terminal speed of $\sim$0 km s^{-1} before it disappeared without a dominant redshift (unlike the filament eruption event "E4," which eventually showed a redshift; K. Namekata et al. 2022c). This puzzling absence of redshift after zero velocity leads to questions about how this eruptive prominence evolved. Indeed, there are various strong observational constraints concerning this event. First, the fact that it was always visible in emission indicates that it was consistently outside the stellar disk. Second, the deceleration rate close to the surface gravity of the star suggests that it was launched from near the stellar surface, aligned somewhat along the LOS. These factors constrain the possible dynamics significantly, leading us to use a simple numerical model to extract more detailed dynamics of this event, as will be shown in Section 3. Additionally, as mentioned in Paper I, simultaneous spectropolarimetric observations at the Télescope Bernard Lyot (TBL) and photometric observations by the Transiting Exoplanet Survey Satellite (TESS, G. R. Ricker et al. 2015) were conducted. The spectropolarimetric observations at TBL have been used for Doppler Imaging (DI) and Zeeman–Doppler Imaging (ZDI), enabling us to reconstruct the spot and magnetic field configurations. Moreover, the TESS light curve shows quasiperiodic variations due to rotation with large starspots, which allows us to extract information on starspot sizes and locations. In summary, we have obtained an unprecedented data set that will help us infer the direction, evolution, and origin of stellar prominence eruptions.

Leveraging this data set, in this study, we examine the dynamics of the prominence and its relationship to starspots and the global magnetic field geometry. In Section 2, we perform the spot and magnetic field mappings by using the above data sets from TBL (Section 2.1) and TESS (Section 2.2). In particular, we get independent intensity maps from both data, which are compared with each other (Section 4.1). In Section 3, we perform simple modelings of the dynamics of the prominence eruptions based on the above strong observational constraints (Section 3.1). We apply the simplest 1D freefall model to the observation (Section 3.2) and later apply a 1D HD simulation of the flow along the expanding magnetic loop (pseudo 2D magnetohydrodynamics (2D MHD) model, see Section 3.3). Finally, we discuss the dynamics and the relationship between prominence eruptions and surface mapping in Section 4.

2. Observations and Models of Starspot and Magnetic Field

2.1. Doppler and Zeeman–Doppler Imaging

Spectropolarimetric observations of EK Dra were recorded at Pic du Midi Observatory using the Neo-NARVAL instrument (A. López Ariste et al. 2022). The time series consists of 18 observations collected in 2022 between March 22 and April 25 (Table 1). From this data set, we discarded two observations suffering from a low signal-to-noise ratio (S/N hereafter), using 16 observations in our analysis. All data were automatically reduced using the default data reduction software of the instrument. The reduced material obtained for each polarimetric sequence results in one intensity (Stokes I) and one circularly polarized (Stokes V) spectrum, covering the whole wavelength domain between 380 and 1050 nm. We noticed that the bluest spectral orders of our observations were plagued by a very low S/N (a similar situation was reported by T. S. Metcalfe et al. 2023, using the same instrumental setup). We, therefore, conservatively decided to ignore in every reduced observation all spectral bins bluer than 470 nm.

As generally done to detect weak, circularly polarized Zeeman signatures dominated by the noise, we used the least-squares deconvolution method (LSD, J. F. Donati et al. 1997; O. Kochukhov et al. 2010) to extract, from each spectrum, an average line profile in Stokes I and V. To do so, we used a list of photospheric spectral lines produced by the VALD database (T. Ryabchikova et al. 2015), using a surface effective temperature and gravity close to the fundamental parameters of EK Dra. We kept for our analysis atomic lines deeper than 40% of the continuum level. We discarded lines in telluric bands and photospheric lines blended with strong chromospheric lines, resulting in 1400 spectral lines for the LSD analysis. The sets of LSD line profiles are displayed in Figures 1 and 2. For most observations, circularly polarized Zeeman signatures can be seen in LSD profiles at the radial velocity of EK Dra (at around -20.3 km s^{-1}).

The next step in the modeling consists of using the whole time series of Stokes I and Stokes V LSD profiles to map the surface brightness of EK Dra (using Stokes I) and its large-scale surface magnetic field (using Stokes V). The Zeeman–Doppler Imaging technique (ZDI hereafter), first described by M. Semel (1989), is employed to perform the tomographic inversion. We used here the ZDI code of C. P. Folsom et al. (2018), in which the surface magnetic field is projected onto a spherical harmonics frame, following the formalism of J.-F. Donati et al. (2006). We assumed an inclination angle $i = 60°$ and a projected rotational velocity $v \sin i = 16.4$ km s^{-1}, taking our values from the ZDI study of I. A. Waite et al. (2017). The rotation phases were calculated assuming a rotation period of 2.766 days (taken from the same authors) and a reference Julian date equal to 2459661.39. Contrary to I. A. Waite et al. (2017), our search for surface differential rotation using the sheared image approach of P. Petit et al. (2002) did not deliver any conclusive results using Stokes V spectra, so solid body rotation was assumed in our model, leading to a reduced χ^2 equal to 1.15. Figure 3 shows the magnetic geometry centered at the rotation phase when the prominence eruption occurred. The modeled Stokes V LSD profiles are overplotted on the observed LSD profiles in Figure 1.

Two main features dominate the complex magnetic geometry reconstructed here. The first one is a strong patch of negative radial field at high latitudes. The second one is a prominent, negative toroidal field component storing 73% of the surface magnetic energy (the presence of this azimuthal field component is readily visible as a symmetric shape of Stokes V profiles, featuring most of the time a central positive lobe surrounded by two negative lobes). The average unsigned surface magnetic field strength is 120 G, while the maximal unsigned field strength reaches 216 G. The field configuration is mostly axisymmetric, as seen in a majority of stars with a predominant toroidal field component (V. See et al. 2015). The general field characteristics obtained with our set of observations in 2022 are in overall agreement with the maps reconstructed with data ranging from 2006 to 2012 by I. A. Waite et al. (2017), who repeatedly reported a negative

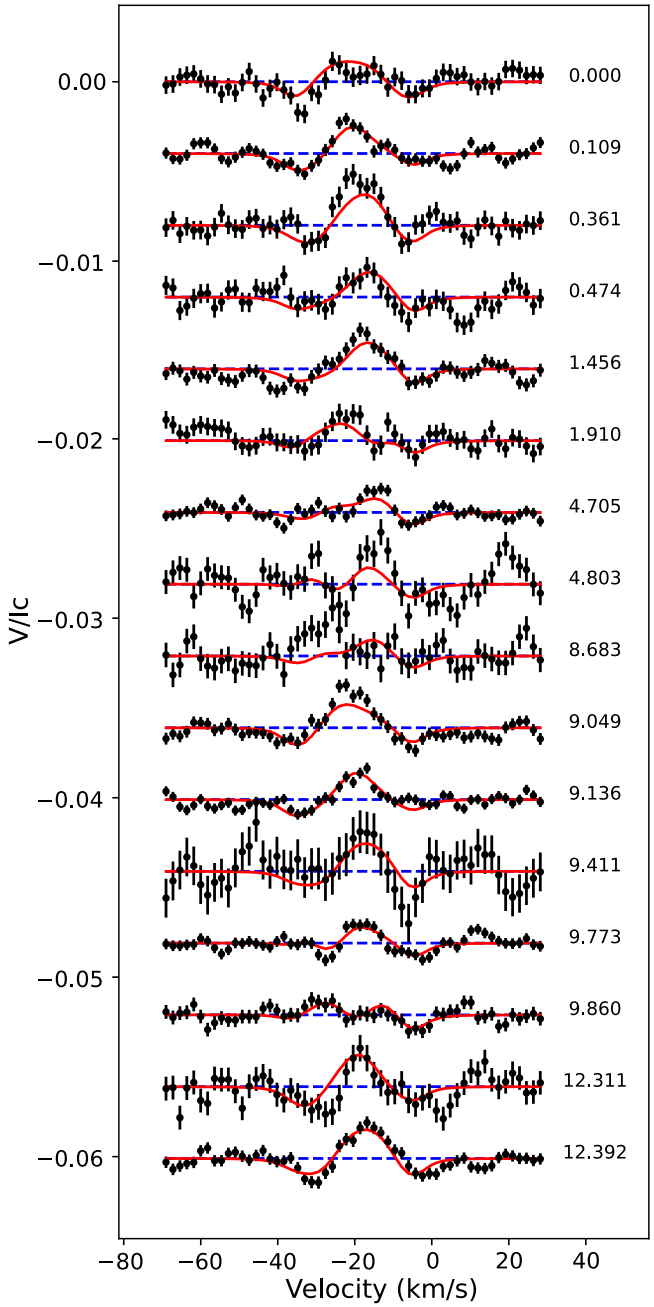

Figure 1. Observed Stokes *V* LSD profiles (back dots) and synthetic LSD profiles produced by the ZDI model (red curves). The blue dashed lines show the zero level. The numbers on the right indicate the rotation cycles. Successive observations are vertically shifted for plot clarity.

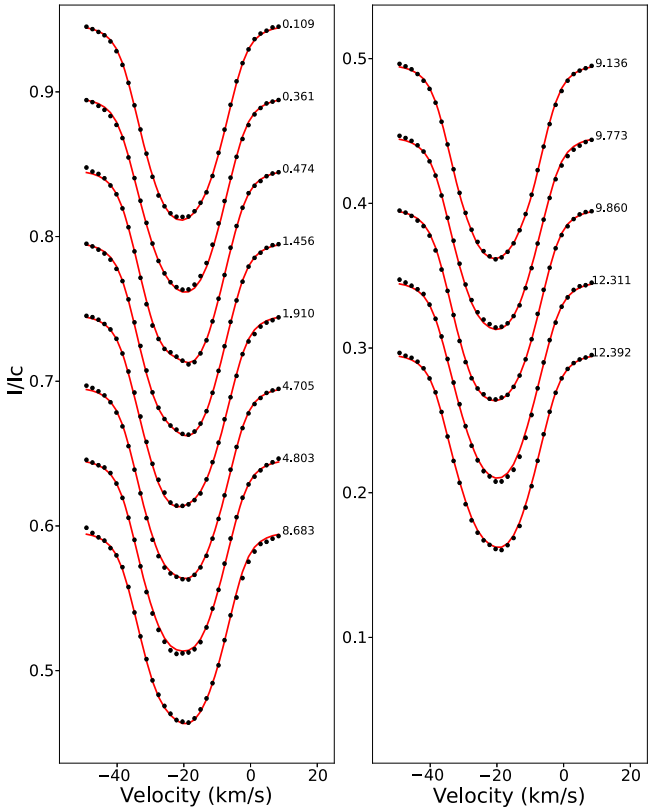

Figure 2. Same as Figure 1, but for the Stokes *I* LSD profiles.

toroidal field and a patch of negative radial field close to the pole. The average field value that we obtain here is, however, about 30% stronger than any average value listed by I. A. Waite et al. (2017).

In Figure 4, coronal extrapolation of the radial surface magnetic field was performed by using a potential field source surface model (e.g., M. D. Altschuler et al. 1977). The distance beyond which the field lines become open is a free parameter of our potential field extrapolation. This parameter can only be estimated through stellar wind modeling, which is beyond the scope of the current paper. In the solar case, a value of $\sim 2.5\,R_\odot$ is usually assumed and is supported by observations of the positions of the coronal holes and streamers (e.g., C. J. Schrijver & M. L. DeRosa 2003; M. L. DeRosa et al. 2012). In the case of stars, this value is unknown and likely depends on the stellar wind properties, as well as other stellar properties such as rotation and magnetic field strength (e.g., A. A. Vidotto et al. 2013; V. Réville et al. 2016). Here, we adopted a value of 3.4 $R_{\rm star}$, as used in other stellar studies (e.g., M. Jardine et al. 2002). therefore, mimicking the effects of a stellar wind blowing open the field lines. This model provides a simple visualization of the open and closed coronal magnetic field, aiding in the interpretation of the relation between the large-scale field geometry and the surface spot features (see Sections 4.1 and 4.2).

Using our set of Stokes *I* LSD profiles in Figure 2, we also reconstructed a brightness map of EK Dra using the DI method (S. S. Vogt & G. D. Penrod 1983, DI hereafter). The brightness model allowed for both dark and bright spots on the stellar surface, similar to, e.g., T. Q. Cang et al. (2020), who used the same code. Figure 5(a) shows the resulting spot distribution centered at the rotation phase when the prominence eruption occurred. The polar region is occupied by the darkest spot on the map. This polar feature is coincident, on the magnetic map, with the patch of strong radial field close to the pole, although the latitudinal extension of the magnetic spot is larger, reaching a latitude of 30°. Most bright spots are gathered at a latitude of about 60°, while lower latitudes are populated by a mix of bright and dark patches. A second DI model (not shown here) was produced with the inclusion of dark spots only, leading to a surface distribution of dark patches very similar to the one obtained when bright features were allowed as well, at the cost of a 5% increase of the χ^2. We also searched again for the signature of differential rotation using the Stokes *I* time series

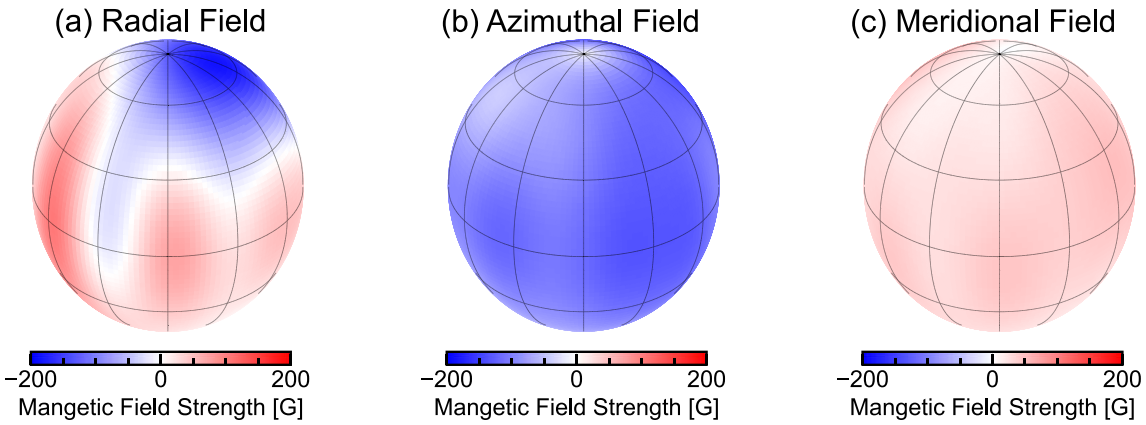

Figure 3. Magnetic field maps on 2022 April 10 for (a) radial, (b) azimuthal, and (c) meridional components. The maps take into account the stellar inclination angle and depict the hemisphere visible from Earth when the prominence eruption occurred (BJD–2459680.033).

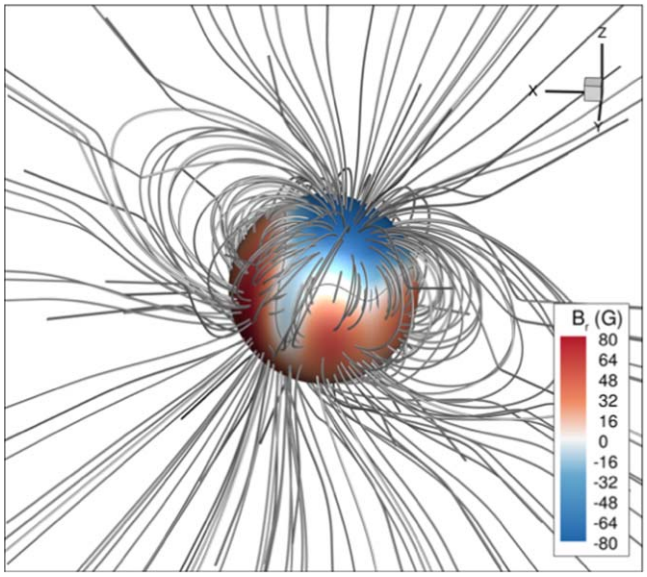

Figure 4. Coronal extrapolation of the radial surface magnetic field using a potential field source surface model (e.g., M. D. Altschuler et al. 1977). Here, we assume that the field becomes open and fully radial beyond 3.4 $R_{\rm star}$, mimicking the effects of a stellar wind blowing open the field lines. The background surface radial magnetic field is the same as Figure 3 and the map depicts the hemisphere visible from Earth when the prominence eruption occurred (BJD–2459680.033).

but failed to identify a unique solution. As for the magnetic map, solid body rotation was therefore assumed here. Most published brightness maps of EK Dra show large spots at high latitudes, as reconstructed here (K. G. Strassmeier & J. B. Rice 1998; I. A. Waite et al. 2017; H. V. Şenavcıet al. 2021), with the notable exception of S. P. Järvinen et al. (2018). However, the high latitude spot is, in most cases, reported to be off-centered with respect to the pole, while the very symmetric configuration reported here is closer to K. G. Strassmeier & J. B. Rice (1998) and H. V. Şenavcıet al. (2021).

2.2. Starspot Mapping from TESS Light Curve

EK Dra (TIC 159613900) was observed by TESS in Sector 50, starting from 2022 March 26 to April 22.[24] In Paper I, the full-frame image data obtained with 10 minutes cadence was processed by using the Eleanor package (A. D. Feinstein et al. 2019). Here we use the "principal component analysis" ("PCA") flux, which has common systematics between targets on the same camera removed.[25] The TESS light curve obtained exhibits quasiperiodic rotational modulation with an amplitude of a few percent, which is attributed to surface starspots. The light curve of EK Draconis is not entirely periodic, indicating the evolution of starspots and/or different periodicities of each starspot due to surface differential rotation.[26]

Here we performed a starspot mapping from the TESS light curve by using the code implemented by our previous study (K. Ikuta et al. 2020). For detailed information on the code, please refer to K. Ikuta et al. (2020). In the following, we provide an overview of the code, including its assumptions and parameters. We set certain stellar parameters as fixed, including the contrast of starspots as 0.27 ($T_{\rm spot} = 4069$ K), which was calculated based on the stellar surface temperature (here we used $T_{\rm eff} = 5700$ K) using the empirical rule from Equation (4) in K. Herbst et al. (2021). The limb darkening law was assumed based on the empirical rules by A. Claret & J. Southworth (2023). The stellar inclination angle i is also fixed as 60° based on previous studies. The code estimates several parameters using the Markov Chain Monte Carlo (MCMC) method (D. Foreman-Mackey et al. 2013; S. Sharma 2017). Despite the vastness of the parameter space, the introduction of the parallel tempering technique (K. Hukushima & K. Nemoto 1996; S. Sharma 2017) allows for comprehensive coverage of this space within a practical time frame. The model for the rotational modulation in TESS light curves employs the macula model (D. M. Kipping 2012), which assumes circular spots with predefined contrast values, and the emergence/decay of these spots are modeled as a linear emergence/decay in the spot area. The free parameters include the equatorial rotation period ($P_{\rm eq}$ in days), the degree of differential rotation (κ), the latitude (ϕ in degrees), the initial longitude (Λ in degrees), the reference time ($t_{\rm ref}$ in days; the midpoint of the interval during which the spot is at its maximum radius), the

[24] https://archive.stsci.edu/missions/tess/doc/tess_drn/tess_sector_50_drn72_v02.pdf

[25] Note that in Paper I, we used the combination of raw flux and smoothed PCA flux to extract the small-amplitude flaring light curve because of the relatively large noise in PCA flux, but here we use the unsmoothed PCA flux.

[26] We understand that the interpretation of periodic variations in the light curves may not be so straightforward, and there are caveats with light-curve fitting (e.g., S. V. Jeffers & C. U. Keller 2009; G. Basri 2018), but here we assume simple starspot modeling.

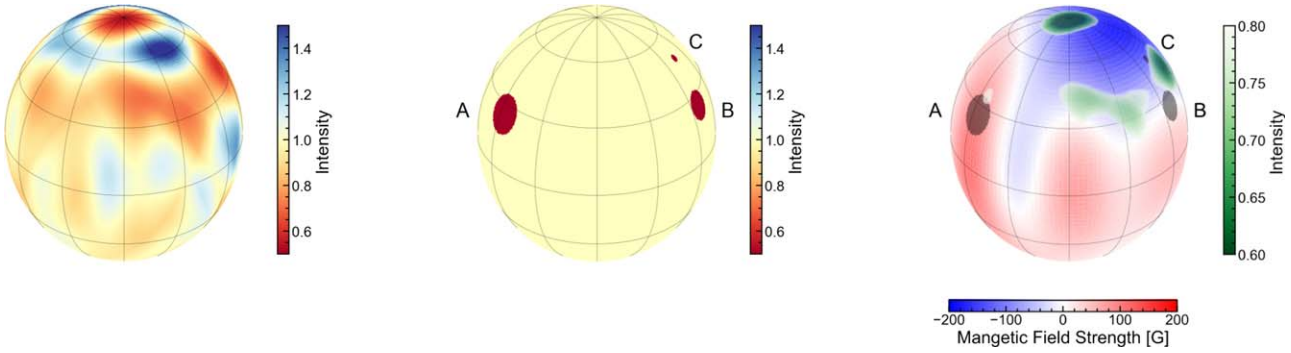

(a) Doppler Imaging (b) TESS Light Curve Modeling (c) ZDI+DI+TESS

Figure 5. Starspot maps on 2022 April 10, from (a) Doppler imaging and (b) TESS light-curve modeling. (c) Comparison of the spots from the Doppler imaging (green, right color bar) and those from the TESS light-curve modeling (gray circles), plotted on the radial magnetic field (background red and blue colors, the same as Figure 3(a)). The hemisphere is the same as Figures 3 and 4, a visible hemisphere when the prominence eruption occurred (BJD–2459680.033). The values in the intensity map are dimensionless as they are normalized by the quiescent surface intensity of the star.

Table 1
The Summary of Spectropolarimetric Observations of EK Dra Using the TBL

UT Date	UT Middle	JD Middle
2022 Mar 22	21:16:41	2459661.3866
2022 Mar 23	04:32:22	2459661.6892
2022 Mar 23	21:15:32	2459662.3858
2022 Mar 24	04:44:13	2459662.6974
2022 Mar 26	21:55:15	2459665.4134
2022 Mar 28	04:03:55	2459666.6694
2022 Apr 4	21:36:01	2459674.4000
2022 Apr 5	04:05:26	2459674.6705
2022 Apr 15	21:40:01	2459685.4028
2022 Apr 16	21:58:57	2459686.4159
2022 Apr 17	03:47:05	2459686.6577
2022 Apr 17	22:01:35	2459687.4178
2022 Apr 18	22:02:39	2459688.4185
2022 Apr 19	03:50:18	2459688.6599
2022 Apr 25	22:31:06	2459695.4383
2022 Apr 26	03:53:10	2459695.6619

maximum radius ($a_{\max}$ in degrees), the emergence duration (in days), and the decay duration (in days).

We exclusively utilized data from TESS Sector 50, spanning approximately 27 days. We removed large stellar flares from the light curve before the modeling. EK Dra was also observed in Sectors 48 and 49, but we limited the used data only to Sector 50, where all of the Hα flare data (see Paper I) and most of the DI/ZDI data were obtained. The reason why we limited the period was because extending the time frame would necessitate the inclusion of more starspots, complicating the resolution of parameter degeneracies and making it more difficult to find the most likely solution with MCMC. To test the impact of using only the limited period on the mapping, we added approximately half of the Sector 49 data to the Sector 50 data and performed the mapping. As a result, the outcomes did not significantly differ. Therefore, the variation in observation time has minimal impact on the results, and we present only the essential data from Sector 50 in this study. In this study, we performed the MCMC sampling with configurations of two and three starspots. Based on the Bayesian criterion "Evidence," the scenario involving three starspots was adopted (K. Ikuta et al. 2020, 2023).

Figure 6 presents a comparison between the TESS light curve and the optimum light curve. While some residuals remain, the overall characteristics of the light curve are well reproduced. It has been reported that increasing the number of starspots could fill in these residuals with smaller spots (K. Ikuta et al. 2023), but even our three-spot model adequately reproduces the general features of the light curve. Table 2 summarizes the estimated spot length scale (radius), latitude, and longitude at the time of the prominence eruption. Other important parameters, such as differential rotation and emergence/decay rates, will be presented in our next paper (K. Ikuta et al. 2024, in preparation); Figure 5 illustrates the configuration of starspots at the time of the prominence eruption. We can see that there are three midlatitude spots (labeled A, B, and C in Table 2), all of which are in the visible hemisphere at this time.

In the following, we compare this result with the DI/ZDI map in Section 4.1 and compare them with prominence eruption in Section 4.2.

3. Observationally Constrained Model of a Prominence Eruption

3.1. Observation Summary

The observational characteristics of the superflare event on the young solar-type star EK Dra are summarized below: The superflare (referred to as "E1" in Paper I) occurred on 2022 April 10 during a multiwavelength observation campaign spanning from 2022 April 10 to April 21. Table 3 summarizes the observational properties of the superflare. The TESS white-light flare exhibited an energy magnitude of 1.5×10^{33} erg, classifying it as a superflare. During the superflare, significant increases in Hα emission were observed. The event was characterized by a strong blueshifted emission in the Hα line, indicating a rapid outward movement of material at LOS speeds reaching up to 690 km s^{-1}. This blueshifted emission was interpreted as the first detection of a prominence eruption from a young solar-type star.

Figure 7 shows an example of the observed Hα line profiles and the temporal changes in velocity (taken from Paper I[27]). In Paper I, as in Figure 7(b), the blueshifted Hα profiles was

[27] In Figures 6(c) and 7(c) of Paper I, the integrated time is described as ±5 minutes, but correctly, it is ±2.5 minutes. Here, we correct this typo.

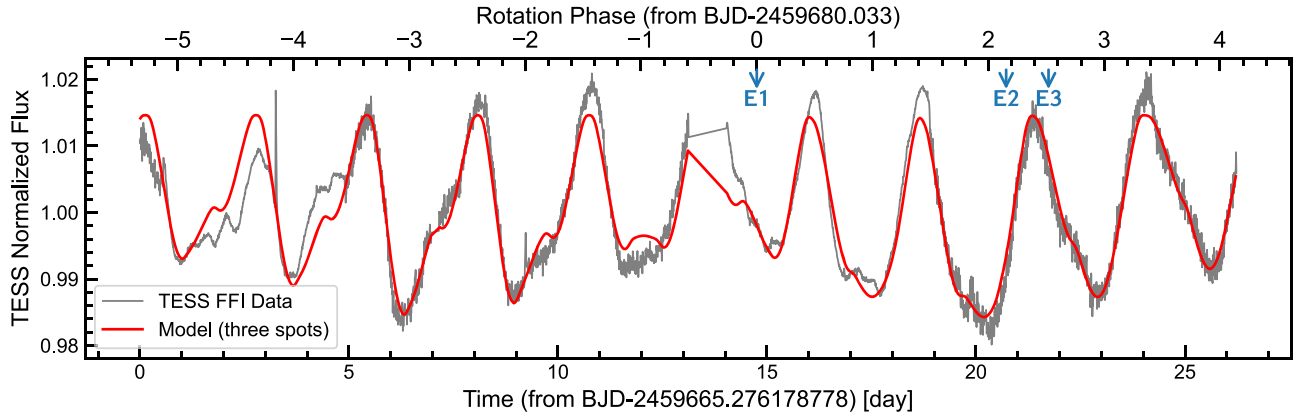

Figure 6. Results from TESS light-curve modeling. The gray line represents the observed data from TESS Full Frame Images (FFI) in 2022 (Sector 50), and the red line shows the modeled light curve, which includes three spots.

Table 2
Spot Parameters on 2022 April 10 from TESS Light-curve Inversion

	Spot A	Spot B	Spod C
Length Scale [10^{10} cm]	$1.02^{+0.08}_{-0.07}$	$0.79^{+0.05}_{-0.07}$	$0.22^{+0.02}_{-0.02}$
(Length Scale [$R_{\rm star}$])	$0.1565^{+0.0001}_{-0.0001}$	$0.1192^{+0.0001}_{-0.0001}$	$0.034^{+0.0001}_{-0.0001}$
Latitude [deg]	$25.06^{+0.08}_{-0.02}$	$25.05^{+0.09}_{-0.02}$	$48.13^{+0.06}_{-0.07}$
Longitude [deg][a]	$-56.84^{+0.01}_{-0.06}$	$67.15^{+0.06}_{-0.01}$	$72.71^{+0.06}_{-0.06}$

Note.
[a] Longitude is defined by setting the prime meridian, which is the meridian at 0°, as the reference point when viewed from the Earth.

analyzed using single Gaussian fitting (hereafter "one-component" fitting) or two Gaussian fitting (hereafter "two-component" fitting) methods for the velocity estimates, depending on the different interpretation of the central component. For the two-component fitting, it is assumed that emissions near the line center originate from flare ribbon emissions, and additional blueshifted emissions are superimposed on the profile. Based on this assumption, the line center component is presumed to have a velocity of zero, making the velocity of the blueshifted component the only free parameter. As a result of these fittings, Figure 7(b) shows two types of velocity evolution. Both methods estimate the maximum LOS velocity[28] of $690 \pm (82-93)\,{\rm km\,s^{-1}}$, which is notable as it approaches the stellar escape velocity $\sim$670 km s^{-1}. The decrease in velocity over time was comparable to the stellar gravity, suggesting that the prominence material's dynamics were influenced by the star's gravitational field. However, after the blueshift lasted for $\sim$20 minutes, the emission component approached $\sim$0 km s^{-1} and eventually disappeared without showing any redshift. The reasons behind the disappearance of the emission at a velocity of zero remained unclear, posing questions about the dynamics.

These observational signatures indicate the following strong constraints on the spatial and dynamic properties of the eruption:

1. First, the presence of an Hα emission profile without any absorption signatures indicates that the prominence was consistently positioned above the stellar limb throughout the eruptive event.
2. Second, the detection of a white-light flare suggests that the flare's footpoints were not entirely obscured by the stellar disk.
3. Additionally, the observed deceleration of the prominence, which aligns closely with the star's surface gravity, implies that the eruption could be oriented nearly along the line of sight.

Based on the above constraints, in Sections 3.2 and 3.3, we will estimate the possible dynamics of prominence eruption, such as the event's location, direction, and evolution, by using two different types of simplified models.

3.2. Simple 1D Freefall Model

As a first approach, we consider a simple model where the prominence center of mass is ejected in a 1D direction and falls solely under the influence of stellar gravity (hereafter referred to as the simple "1D freefall" model). It should be noted that this is not a complete "freefall" scenario, as it does not take into account the gravitational forces perpendicular to the path of motion. In the case of the Sun, the ejection of prominences is influenced by the configuration of magnetic field lines. Some erupted prominences land on another point of the solar surface, but others return near their original footpoints along magnetic lines. This case is poorly understood for stellar eruptive events; therefore, to avoid complexities arising from the lack of observational constraints on the stars, we have adopted this simplified approach. Our study is the first attempt at this kind of dynamical modeling among stellar flare/prominence eruption observations. This is because of our well-defined characteristics of the stellar prominence eruptions, as summarized in Section 3.1.

Observations provide a well-defined time variation of LOS velocity of prominence center-of-mass $v_{\rm LOS}(t)$. To reproduce $v_{\rm LOS}(t)$ using the schematic model described in Figure 8, which satisfies conditions 1–3 mentioned above, we estimate the optimal values of the following four parameters using an MCMC:

1. h_0: Initial height of the prominence at $t = t_0$, where $h_0 > 0$,
2. ϕ: The angle of prominence eruption direction against the LOS direction of the observer, where $0 < \phi < \pi/2$,
3. α: The angle of initial prominence direction against stellar limb direction, where $0 < \alpha < \pi/2$
4. v_0: Initial LOS velocity ($t = t_0$).

[28] In Paper I, there was a typo in that the error bars were described as $690 \pm$ (92–93) km s^{-1} in some parts. Here, we correct this typo.

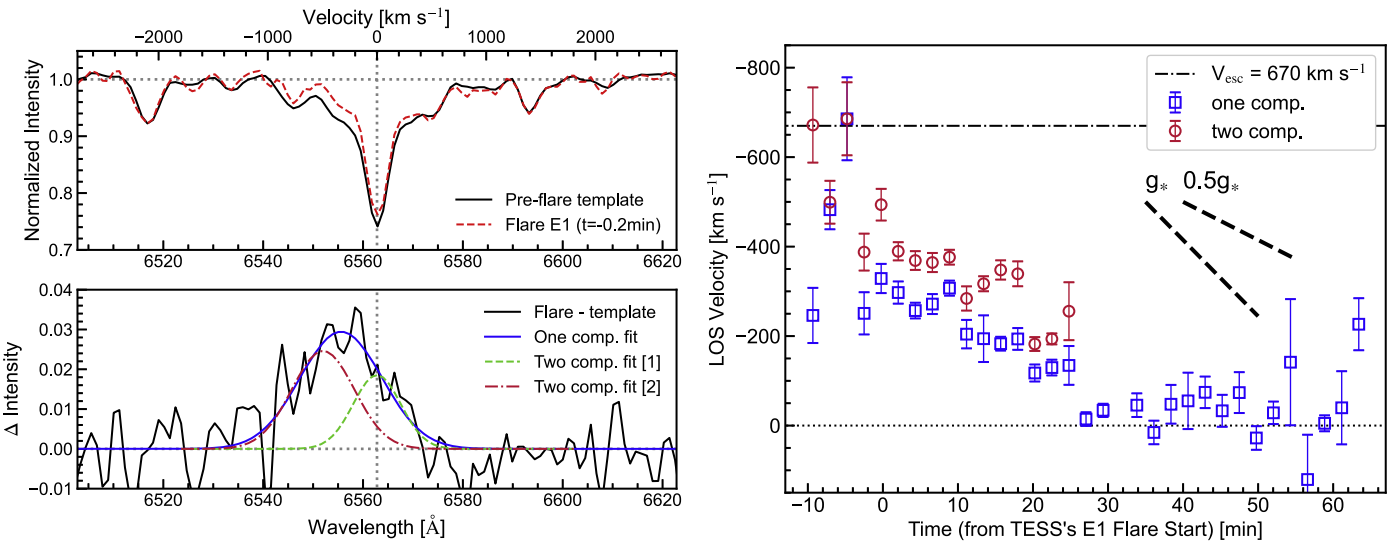

(a) (b)

Figure 7. An example of (a) the blueshifted Hα spectra and (b) the time evolution of the velocity taken from Paper I.

Here, in the case of the one-component fit for Hα line profiles (see Section 3.1), the used time range is $t_0 = -0.23$ minutes $< t <$ 52.03 minutes for optimizing, and in the case of the two-component fit, the range is $t_0 = -0.23$ minutes $< t <$ 24.79 minutes. As for the one-component fit data, before time -0.23 and after 52.03 minutes, the signal was weak, resulting in a large error in velocity, so we did not include these periods. As for the two-component fit data, after 24.79 minutes, the residual asymmetric components were not obtained.

In the schematic picture in Figure 8, the distance $r(t)$ from the center of the star and the angle $\delta(t)$ between the radial direction and the direction of the eruption at a given time t and the distance traveled along a straight line from the initial point x ($=x(t)$) (see Figure 8) can be expressed as follows:

$$r(x) = (x^2 + (h_0 + R_{\rm star})^2 + 2x(h_0 + R_{\rm star})\sin(\phi + \alpha))^{\frac{1}{2}} \quad (1)$$

$$\cos\delta(x) = \frac{x^2 + r(x)^2 - (h_0 + R_{\rm star})^2}{2xr(x)}. \quad (2)$$

The equation to be solved is,

$$\frac{d^2x}{dt^2} = -\frac{GM}{r(x)^2}\cos\delta(x). \quad (3)$$

Here, G is the gravitational constant, (6.67×10^{-8} cm^3 s^{-2} g^{-1}), M is the stellar mass ($0.95\,M_\odot$), and $R_{\rm star}$ is the stellar radius ($0.94\,R_\odot$). Equation (3) can be solved under a given initial condition of h_0, ϕ, and α by using the fourth-order Runge–Kutta method. We performed parameter estimations by using the adaptive MCMC methods (T. Araki & K. Ikeda 2013; D. Foreman-Mackey et al. 2013). The number of chains is 10,000, and the burn-in sample size is 2000.[29] The acceptance ratio of the MCMC chain is approximately 0.25. The proposal distribution is tuned during the first burn-in 2000 chain with the adaptive methods.

Boundary conditions are set as

1. $(h_0 + R_{\rm star})\cos\alpha > R_{\rm star}$: The prominence should be outside the stellar limb from the observer's view,
2. $0 < h_0 < 2R_{\rm star}$, $0 < \phi < \pi/2$, and $0 < \alpha < \pi/2$.

In Paper I we learned that the initial deceleration (0.34 ± 0.15 km s^{-2}) was almost entirely surface gravity (0.30 ± 0.05 km s^{-2}). This indicates that the initial height of the eruption is relatively close to the stellar surface. If we assume the initial height as $h = 2R_{\rm star}$, the gravitational deceleration becomes one-fourth, making it unlikely that this is the initial position. So we set the boundary condition for the initial height at two stellar radii, but changing this condition did not significantly affect the results.

Then we performed two different MCMC runs for the velocity evolution, which are obtained by one- and two-component fitting of the blueshifted Hα spectral line profile. Figures 9(a) and (b) show the results of the sampling for the one- and two-component fitting cases, respectively. The estimated parameters are summarized in Table 4. Figure 10 compares the observed velocity variations with the modeled one based on the estimated optimal parameters. The figure confirms that the model curve corresponds well with the observed data points. From these estimation results, in both cases, a generally similar picture of the eruption is presented:

1. the eruption originates near the stellar surface (0.045–0.07 $R_{\rm star}$),
2. it erupts in a direction approximately 15°–24° from the line of sight, which is relatively close to the line of sight, and
3. it erupts from a point close to the limb at an angle of 12°–16° from the limb.

Of course, in reality, the direction of the ejection may not be linear, and the prominence likely has a spread-out structure

[29] Burn-in sample size refers to the initial samples in an MCMC simulation that are discarded to minimize the influence of the starting point. This allows the chain to converge to the target distribution. The acceptance ratio is the fraction of accepted steps, indicating the chain's efficiency. A balanced ratio (often ∼20%–30%) ensures effective exploration of the parameter space.

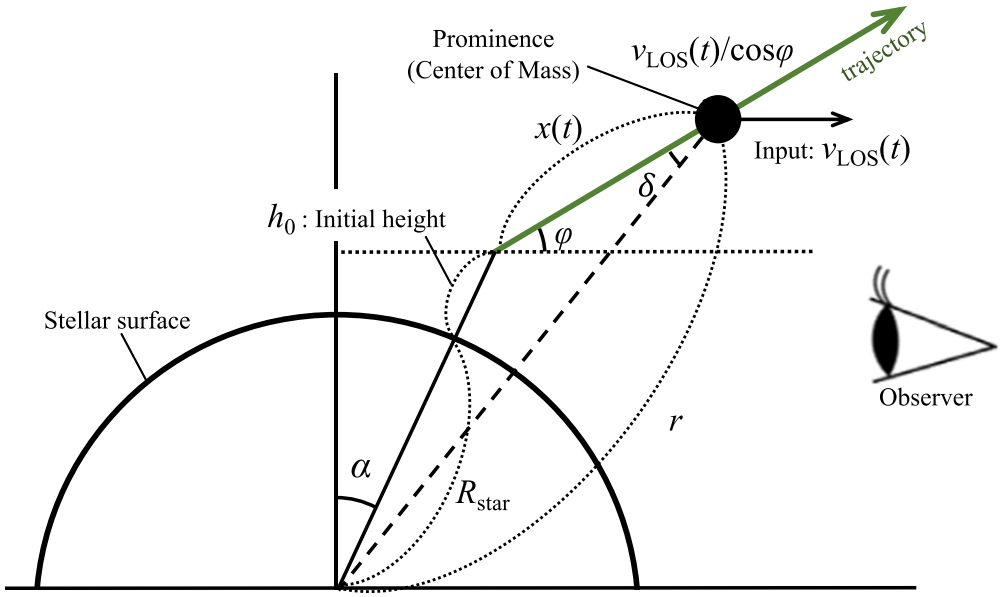

Figure 8. Schematic picture of the simple "1D freefall" model.

Table 3
Summary of Length Scale and Area of the Superflares, Prominence/Filament Eruptions, and Starspots on EK Dra Estimated in Paper I

Date (ID)	BJD	Blueshift	Flare Loop (10^{10} cm)	Prominence (10^{10} cm)	Spot (10^{10} cm)	Rot. Phase [0–1]	LC Profile
2022 Apr 10 (E1)	2459680.033	Yes	0.73	8.3–300	2.1 (0.22–1.02)[a]	0.00	Decline-Loc.min
2022 Apr 16 (E2)	2459685.998	Yes	1.16	1.4–51	2.4	0.15	Rise
2022 Apr 17 (E3)	2459687.012	No	0.67	⋯	2.4	0.51	Decline
2020 Apr 5 (E4)	2458945.241	Yes	0.48	1.4–40[b]	1.9[c]	0.73[d]	Loc.max
2020 Mar 14 (E5)	2458923.004	No	1.50	⋯	2.3[c]	0.70[d]	Decline

Notes. The table data is taken from Paper I. "Rotation Phase" is the timing when the superflares occur relative to the stellar rotational phase. Here, rotational phase 0 is defined as 2459680.033, and rotational period $P_{\rm rot}$ is defined as 2.77 days (i.e., phase = ((BJD–2459680.033) mod $P_{\rm rot}$)/$P_{\rm rot}$). As a reference, the stellar radius is 0.94 times the solar radius $\sim 6.55 \times 10^{10}$ cm, and the stellar disk area is $\sim 13.5 \times 10^{21}$ cm^2.

[a] The spot length scale from the TESS light-curve modeling, as described in Table 2.

[b] There was a mistake in the estimation of the upper limit of the length scale in Paper I, so we revised it here.

[c] The spot length scales of E4–E5 events are recalculated to follow the calculation of E1–E3 events, i.e., the local maximum minus the local minimum of the light curve over one rotation containing a flare. However, since the E4 event includes a flare around the local maximum, the maximum value was defined as the top 98% of brightness within one rotation.

[d] Given that the observations are conducted 2 yr apart from the reference time, these values can be meaningless considering the change in spots and differential rotation. "LC Profile" is the light-curve profile when the superflare occurs. "Loc.min" and "Loc.max" are the local minimum and local maximum of the light curve, respectively, and "Rise" and "Decline" are the rising and decline phases of the light curve, respectively.

relative to its center of mass, so it is important to keep in mind that this model is a highly simplified representation. However, there have been no studies that could infer information such as the direction of stellar eruptions to this extent, and this work could serve as a basis for more sophisticated model calculations. In Section 3.3, we attempt to reproduce the observations using a more refined 1D HD simulation of the flow along the expanding magnetic loop (pseudo 2D MHD model), based on the constrained information obtained here.

3.3. 1D HD Simulation of the Plasma Flow along an Expanding Magnetic Loop (Pseudo 2D MHD Model)

Here we present the results of the 1D HD simulation of the plasma flow along an expanding magnetic loop (a pseudo 2D MHD model), emulating the dynamics of a prominence eruption, by using the methodology employed by K. Ikuta & K. Shibata (2024). This is also a simple but more sophisticated model than that described in Section 3.2, which is based on a solar prominence eruption model. The aim of this simulation is to investigate whether the observed dynamic spectrum of Hα, i.e., the velocity change, can be explained by a simple hydrodynamic model, whose initial conditions are constrained on the basis of the results in Section 3.2.

In this model, the shape and time variation of the magnetic field configuration is assumed on the basis of an approximate version of the self-similar magnetohydrodynamic outflow for a typical model of CME (e.g., K. P. Dere et al. 1997; M. J. Aschwanden 2017; see also theoretical self-similar CME model developed by B. C. Low 1984; S. E. Gibson & B. C. Low 1998). Figure 11 shows the assumed magnetic loop expansion model. The plasma velocity along an expanding magnetic loop (due to gravity and gas

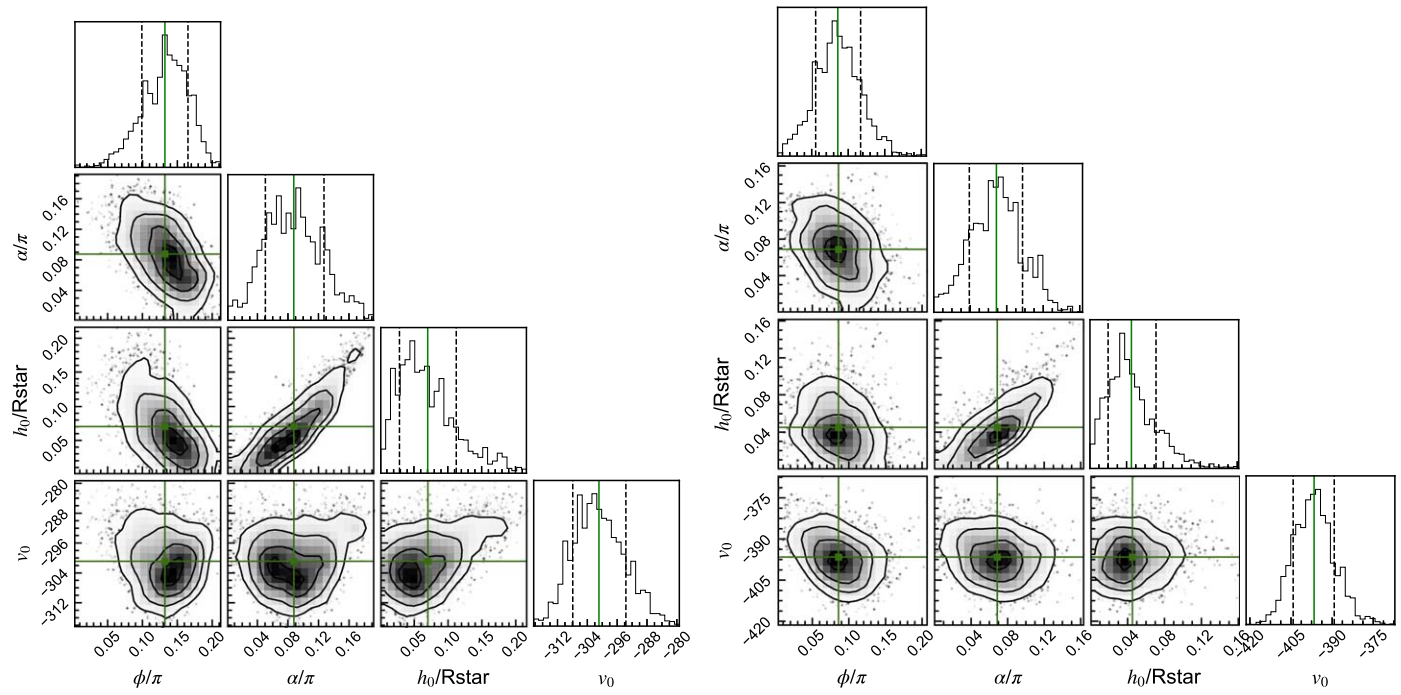

Figure 9. Correlations between posterior samples for each parameter for the "1D freefall" model (Section 3.2). Panels (a) and (b) show the MCMC sampling results for the velocity evolution obtained by the one- and two-component fitting of the Hα line, respectively. The green line represents the central value obtained by fitting the histogram to a normal distribution using scipy.stats.norm.fit. The black dashed lines indicate the 16% and 84% regions of the distribution. These boundaries correspond to the 68% confidence interval, commonly used to represent parameter uncertainty in MCMC analysis. The figure is plotted with a corner in Python.

pressure) is simulated, whereas the plasma velocity normal to the magnetic field line is assumed to be given based on a model of an expanding loop whose initial velocity is a free parameter which is determined from comparison with observations. Therefore, we can call this a "pseudo 2D MHD model" for prominence/filament eruption. This model nicely captures the motion of the erupting prominence/filament, which is decelerated by gravity after ejection and falls along the erupting magnetic field line in the case of a solar erupting prominence/filament (K. Ikuta & K. Shibata 2024).

Here we assume the configuration of a bipolar magnetic field by two line currents and introduce bipolar coordinates defined by this bipolar magnetic configuration as in K. Shibata (1980). The parameters of the loop configuration are (1) the half distance between the two line poles, which corresponds to the size of an active region at the loop bottom, a, (2) the initial height of the loop top, $y_{\rm int}$, and (3) the initial normal velocity of the loop top, $V_{\rm top}$. We also assume that there is a cool and dense prominence with a uniform temperature of 10^4 K and density of 10^{-13} g cm^{-3} in a localized region in the loop where the curvilinear coordinate parameter v is between $v_{\rm min}$ and $v_{\rm max}$ ($0 < v_{\rm min} < v < v_{\rm max} < 3$) at the initial magnetic loop. The assumed density is consistent with solar observations (10^{-14}–10^{-12} g cm^{-3}; T. Hirayama 1986). Then, the uniform pressure is given by 0.166 dyn cm^{-2}. For the outside of the prominence in the magnetic loop, we assume that there is a hot corona with a temperature of 10^6 K and density of 10^{-15} g cm^{-3}, whose pressure is balanced with the prominence (see K. Ikuta & K. Shibata 2024, for discussion of these assumptions).

As a result of this numerical simulation, we can obtain the time evolution of the temperature, density, and velocity of the plasma inside the 1D loop. To model the effects of different observer perspectives, we introduce a viewing angle parameter θ, which represents the angle between the observer's LOS and the direction of the ejection. For simplicity, we only consider the model viewed from the plane of the 2D magnetic loop. Based on the results obtained in Section 3.2, we adopted $\theta = 90°$ (see Figure 11). While it is possible to slightly change the angle, we did not adopt this approach because, due to the nature of the model, even a small tilt in the angle causes the falling plasma to be projected onto the disk surface, resulting in an absorption profile. However, in future work, we will conduct a broader parametric study.

To compare the model with observations, we calculated the LOS velocity component at each point of the loop. Then, we summed up the mass of the prominence material (plasma with temperatures less than 3×10^4 K) and derived the mass distribution as a function of velocity, simulating the pseudo-Hα spectrum under the optically thin condition. Further radiative transfer calculations were not conducted in this study. Instead, we scaled this modeled dynamic spectrum and compared only its velocity variations with the observations of EK Dra.

As a result of the parameter survey, the optimal parameters that best match the observations were determined as follows: (a, $y_{\rm int}$, $V_{\rm top}$, $v_{\rm min}$, $v_{\rm max}$) = (2.5×10^4 km, 6.0×10^4 km, 5.0×10^2 km s^{-1}, 0.35, 0.75). The assumed velocity of the magnetic loop is plausible, as the typical Alfvén speed in stellar coronae is on the order of 1000 km s^{-1} (K. Shibata & T. Magara 2011). The orange line in Figure 11 (top) illustrates the assumed location of prominence material (based on the above parameters $v_{\rm min}$ and $v_{\rm max}$) in the expanding magnetic loop and its time evolution. As observed in K. Ikuta & K. Shibata (2024) and in Figure 11, we assume that the prominences are predominantly distributed on one wing of the

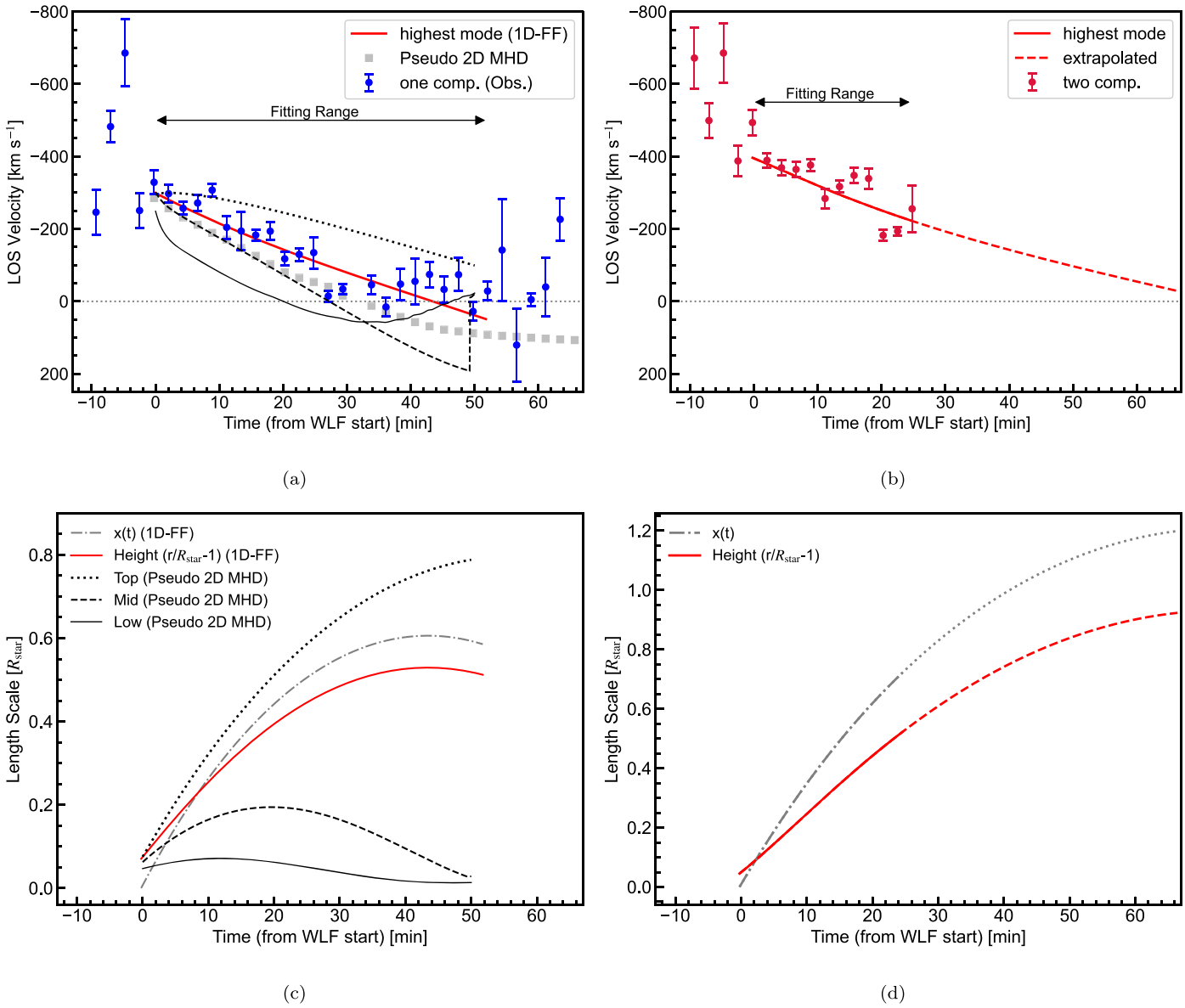

Figure 10. The velocity and length scale evolution with the estimated parameters from the 1D freefall model ("1D-FF"). The panels (a) and (b) represent the time evolution of velocity for the one-component and two-component fit for Hα line profiles, respectively. The modeled time evolution with the most likely parameters is indicated with a red solid line and its extrapolation with the red dashed line. The time range used for MCMC sampling is indicated with arrows. The panels (c) and (d) represent the time evolution of the $x(t)$ (gray dashed–dotted line) and the prominence height (red solid line) for the one-component and two-component fit for Hα line profiles, respectively. For reference, panels (a) and (c) depict the components at three locations within a 1D hydrodynamic simulation of the flow along the expanding magnetic loop ("Pseudo 2D MHD" model; K. Ikuta & K. Shibata 2024 and K. Ikuta et al. 2024, in preparation) from Figure 11 using black lines (the line styles are consistent with those in Figure 11). Additionally, in panel (a), the center positions of the Gaussian fits to the pseudo Hα from Figure 11(c) are indicated by gray squares.

magnetic loop (that is expanding toward Earth), which is often observed in the Sun. In this setup, the prominence is initially ejected, seemingly pushed by the expanding loop, but is then observed to fall back toward the star along the loop. This behavior is consistent with the filament eruption case described by K. Ikuta & K. Shibata (2024). Figure 12 shows the comparison between the modeled pseudo-Hα dynamics spectrum and the observed Hα dynamics spectrum. The overall features of the observation and model look similar to each other, indicating that our model successfully reproduces the observed behaviors to some extent. It should be noted, however, that the final velocities in our model show a redshifted component offset by several tens of km s^{-1}, which is not seen in the observations. In addition, the very fast and faint component of $>$600 km s^{-1} was not well reproduced in this model and the model in Section 3.2. This discrepancy may suggest minor deviations from the model's ability or just a change in the Hα luminosity of the prominence, which will be further discussed in Section 4. Further adjustments to the simulation parameters may be required to refine the alignment with observed data and to explore the underlying causes of these velocity offsets, compared with a solar prominence eruption (K. Ikuta et al. 2024, in preparation).

Figure 10 compares the velocity and height of prominences in the 1D HD model with those in the 1D freefall model discussed in Section 3.2. According to this comparison, both

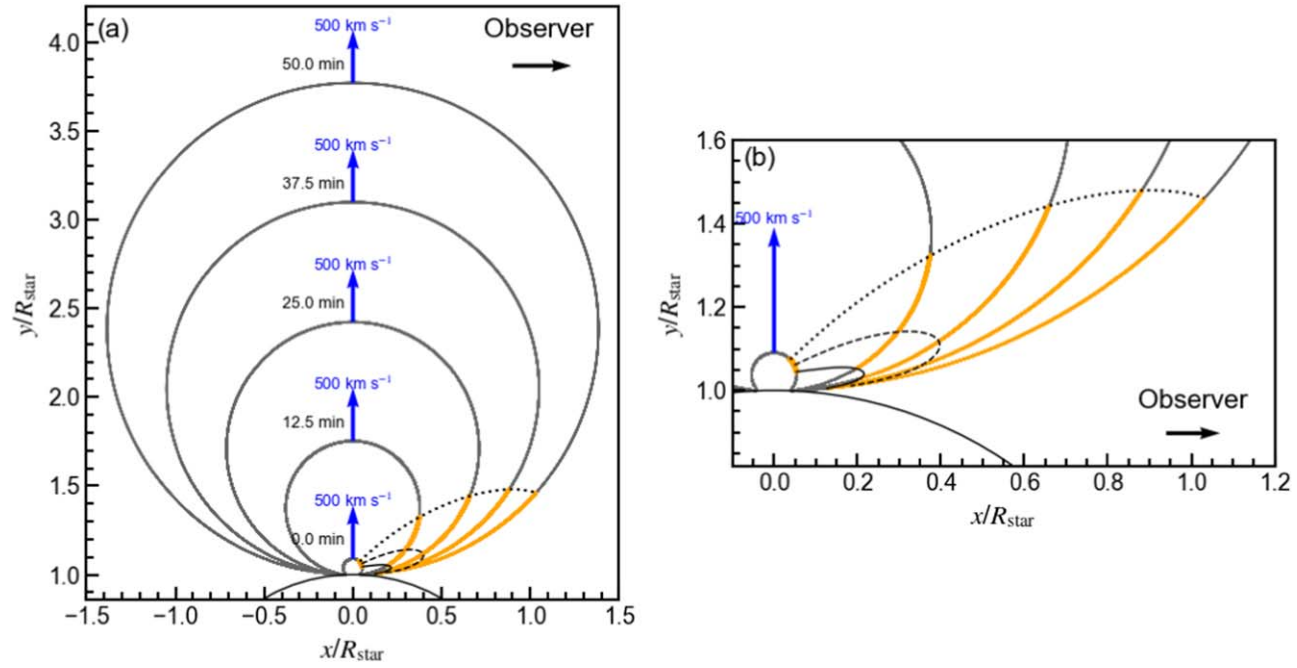

Figure 11. Results from a 1D hydrodynamic simulation of the flow along the expanding magnetic loop (pseudo 2D MHD model; Section 3.3) described in K. Ikuta & K. Shibata (2024) and K. Ikuta et al. (2024, in preparation). (a) Schematic representation of the magnetic loop expanding at a constant velocity (depicted as a looplike structure at different times). The observer's direction is indicated by the black axis. The loop's footpoints are connected to the star, located at the stellar limb. The direction of the eruption is perpendicular to the line of sight. The prominence material in the loop is indicated with orange. The Lagrangian trajectory of plasma at the bottom, middle, and top of the original prominence are indicated with black solid, dashed, and dotted lines. (b) Expanded picture of panel (a). The initial condition of the magnetic loop and explanations of parameters are described in Appendix A.

Table 4
Deduced Parameters for Kinematics of Eruptive Prominence in the Schematic Model of Figure 8

Parameters	Input	Prior Dist.	Proposal Dist.	Estimates from Posterior	
				(A) One Comp.	(B) Two Comp.
Initial Height h_0 [$R_{\rm star}$]	$0.1R_{\rm star}$	$\mathcal{U}(0, 2R_{\rm star})$	$\mathcal{N}(\mu, \sigma^2)$	$0.070^{+0.042}_{-0.042}$	$0.045^{+0.027}_{-0.025}$
LOS angle ϕ	0.1π	$\mathcal{U}(0, \pi/2)$	$\mathcal{N}(\mu, \sigma^2)$	$0.132^{+0.033}_{-0.033}\pi$ (24^{+6}_{-6} deg)	$0.086^{+0.031}_{-0.030}\pi$ (15^{+6}_{-5} deg)
Angle α	0.1π	$\mathcal{U}(0, \pi/2)$	$\mathcal{N}(\mu, \sigma^2)$	$0.088^{+0.040}_{-0.037}\pi$ (16^{+7}_{-7} deg)	$0.069^{+0.029}_{-0.030}\pi$ (12^{+5}_{-5} deg)
LOS Velocity v_0 [km s^{-1}]	$v_{\rm in}$	$\mathcal{U}(v_{\rm min}, v_{\rm max})$	$\mathcal{N}(\mu, \sigma^2)$	-301^{+7}_{-7}	-397^{+7}_{-8}

Note. $\mathcal{U}(a, b) = 1/(b - a)$ is Uniform distribution. $v_{\rm min} = -378$ km s^{-1} and $v_{\rm max} = -278$ km s^{-1} for (A) one-component fit model, while $v_{\rm min} = -500$ km s^{-1} and $v_{\rm max} = -300$ for (B) two-component fit model. $\mathcal{N}(\mu, \sigma^2)$ is a normal distribution. σ is different for each parameter. We defined the center of a posterior distribution fit with a normal distribution as the most likely value. The error range is determined by the region from the 16th to the 84th percentile of the posterior.

models agree within the range of diversity in height and velocity changes predicted by the 1D HD model. The prominence center velocities in the 1D HD model are slightly slower, which consequently results in slightly lower achieved heights. This outcome supports the validity of both models.

4. Discussion

4.1. Starspots and Magnetic Field Topology from Light-curve Inversion and (Zeeman) Doppler Imaging

Here, we compare the spot maps from TESS light-curve modeling with those derived using DI. The TESS light-curve modeling results depicted in Figure 5(b) reveal that during a prominence eruption, all three hypothesized spots were located on the hemisphere visible from Earth. These are designated as spots A, B, and C, and their properties are summarized in Table 2. The result indicates their presence primarily in midlatitudes (25°, 25°, and 48°), although we should keep in mind that the light-curve modeling has inherent limitations, such as the degeneracy between latitude and spot area. Additionally, these spots were positioned near the limb as viewed from Earth (∼20°–30° from the limb). During the observation, spots A and B maintained a significant area, whereas spot C was notably smaller. Note that these are temporally evolving spots, and the minimal area of spot C at this time does not imply it is always small.

The DI results shown in Figure 5(a) reveal large, dark regions suggestive of significant spots at midlatitudes (the latitude of 30°–40°). This is consistent with those observed in the TESS light-curve modeling in Figure 5(b), although the DI map shows more extended spot distributions. This consistency between the two methods validates their spot configuration results. While the TESS light-curve inversion traces time variations, DI does not, resulting in an average spot distribution over a month. Therefore, the two methods are not necessarily identical or completely equivalent, but the obtained consistency may suggest that the spot location (at least the active latitude) does not change significantly within a month. This indication is

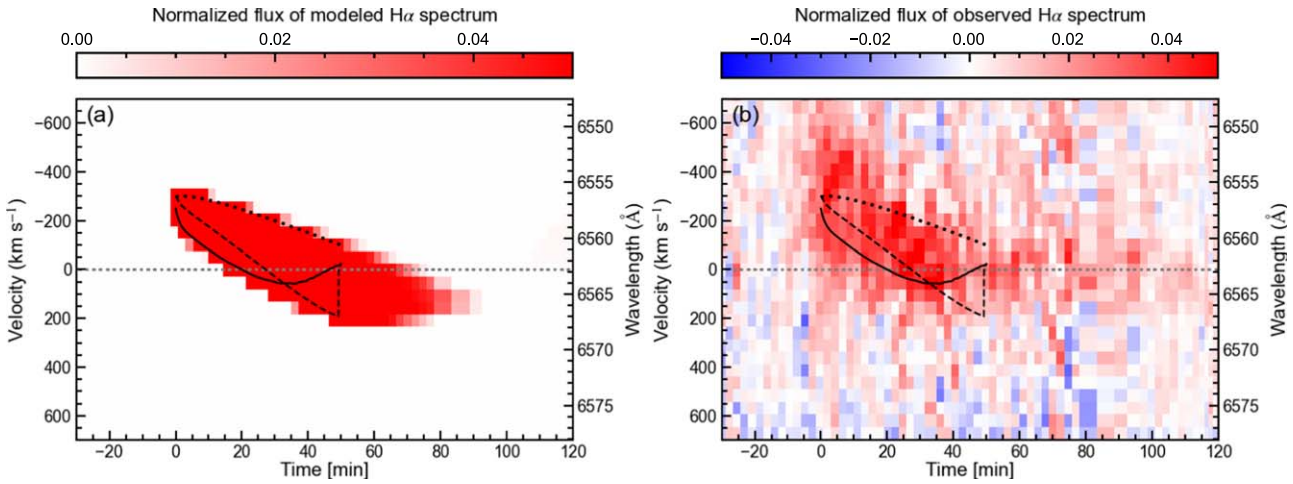

Figure 12. Comparison between the modeled and observed dynamic spectrum of Hα line from a 1D hydrodynamic simulation of the flow along the expanding magnetic loop (pseudo 2D MHD model; Section 3.3). (a) Simulated dynamic spectrum of the Hα line from the prominence material. Each black line corresponds to the velocity evolution of each Lagrangian trajectory of plasma in panel (a) of Figure 11. (b) Observed dynamic spectrum of the Hα line during the giant prominence eruptions on EK Dra, as reported in Paper I.

consistent with the fact that the lifetime of giant starspots on solar-type stars extends to several months to a year (K. Namekata et al. 2019, 2020).

In contrast to the TESS light-curve inversion, the DI results also suggest the presence of a substantial polar spot (see Section 2.1). This is a feature undetectable by TESS light-curve modeling, as stellar rotation does not affect the brightness variation due to such polar spots. Thus, the discrepancies between the two methods in terms of polar spots are not contradictions but rather demonstrate how our complementary observations with DI can compensate for the limitations of TESS light-curve modeling. A detailed global mapping comparison will be addressed in our future work (K. Ikuta et al. 2024, in preparation). In this paper, we focus on the spot locations during a prominence eruption as a snapshot in time.

Figure 3 shows the magnetic field distribution obtained via ZDI. The ZDI's spatial resolution is at least 20°–25° (see Appendix B). Also, we need to keep in mind that ZDI maps tend to cancel out small-scale magnetic fields. So, it is important to recognize that the map primarily reflects the distribution of large-scale magnetic fields rather than local spot's magnetic fields. The radial magnetic field at the poles displays an almost negative unipolar configuration, suggesting that the large polar spots in the DI map (Figure 5(a)) are either associated with a unipolar magnetic field or situated within a large-scale dipole or open magnetic field structure, like a coronal hole. To verify this, we performed a simple field extrapolation using a potential field source surface model (Figure 4) and found that a substantial part of the unipolar negative field at the polar region hosts open magnetic field lines. On the other hand, near midlatitudes, the substantial spots labeled A and B are located near a polarity inversion line (PIL). In Figure 5(c), in more detail, the large starspot B region on the western limb is clearly located on the PIL. Although the starspot A region on the eastern limb is not precisely on the PIL, considering the spatial resolution, it might be associated with the PIL. The existence of these spots in different magnetic environments implicates their potential role in influencing the likelihood of CME launches or the presence of preflare giant prominences, which is discussed in Section 4.2.

4.2. The Origin of Gigantic Prominence Eruption from EK Dra on 2022 April 10

Here we explore the relationship in the locations of starspots, magnetic fields, and prominence eruptions. We focus on the possibility that the superflares and major prominence eruptions are linked to large starspots observed in EK Dra, while prominence eruptions could occur in quiet regions, like solar cases. We begin by synthesizing information regarding the distribution of prominence eruptions, large starspots, and the magnetic field configuration:

1. Eruptive prominences are likely ejected from the footpoints located approximately 12°–16° from the stellar limb (Sections 3.2 and 3.3).
2. These footpoints coincide with a polar region starspot hosting unipolar large-scale magnetic fields and open coronal fields, as well as midlatitude large spots (A and B) hosting large-scale PILs and closed coronal fields (Section 4.1).

The consistency suggests that the massive prominence eruption on 2022 April 10 can be associated with the observed giant starspots.

In the case of the Sun, large prominences are often observed along PILs. Based on this, it can be expected that midlatitude spots with extensive PILs could be the sites of the eruptive prominence. It should also be noted that these regions would have an overlying closed magnetic field, as seen in the coronal field extrapolation presented in Figure 4. An overlying large-scale dipolar magnetic field can suppress the ejected structure, as indicated in the numerical studies of J. D. Alvarado-Gómez et al. (2018). These authors demonstrated that, for a solar-type star with a 75 G dipolar field, escaping CMEs would have kinetic energies $\gtrsim 3 \times 10^{32}$ erg. Because the estimated kinetic energy of the prominence eruption $5.8^{+12.8}_{-4.0} \times 10^{34}$ erg derived in Paper I is much higher than this threshold (see Table 5), the massive prominence eruptions and related CMEs might not be suppressed significantly (see, e.g., K. M. Strickert et al. 2024). Note that the observed average magnetic field of EK Dra of 120 G is slightly stronger than the 75 G, and its magnetic topology is not a dipole, so the applications of the study by J. D. Alvarado-Gómez et al. (2018) could be not so

Table 5
Summary of Energy Distribution of Superflares on EK Dra Estimated in Paper I

Event ID	$fE_{\rm mag}$ (10^{33} erg)	$E_{\rm WLF}$ (10^{33} erg)	$E_{\rm X}$ (10^{33} erg)	$E_{\rm kin}$ (10^{33} erg)
E1	34	$1.5_{\pm 0.1}$	⋯	58^{+128}_{-40}
(norm.)[a]	(1)	(0.043)	(⋯)	$(1.7^{+3.7}_{-1.2})$
E2	54	$12.2_{\pm 0.2}$	$12.3^{+0.3}_{-0.5}$-$16.7^{+0.4}_{-0.7}$	$1.2^{+2.7}_{-0.8}$
(norm.)[a]	(1)	(0.228)	(0.230-0.312)	$(0.022^{+0.050}_{-0.015})$
E4	29	$2.0_{\pm 0.1}$	⋯	$0.35^{+1.40}_{-0.30}$
(norm.)[a]	(1)	(0.068)	(⋯)	$(0.012^{+0.048}_{-0.010})$

Notes. The table data is taken from Paper I. $E_{\rm WLF}$ is white-light flare energy, $E_{\rm X}$ is X-ray flare energy, and $E_{\rm kin}$ is the kinetic energy of eruptive prominence. The free magnetic energy $fE_{\rm mag}$ is estimated by the equation of $fE_{\rm mag} = \frac{1}{8\pi} fB^2 L^3_{\rm spot}$ (e.g., K. Shibata et al. 2013), where a filling factor f is 0.1 and averaged surface magnetic field strength of spot is 1000 G. Not that in Paper I the free magnetic energy was mistakenly estimated under the f value of unity, which significantly overestimated the free magnetic energy by an order of magnitude. Here we correct the values.
[a] The columns "norm." mean the values normalized by the free magnetic energy $fE_{\rm mag}$.

straightforward and there could be some differences for this threshold. A future modeling effort based on the observed magnetic field of EK Dra is required for the exact evaluation.

The polar spot we detected is located in a region of almost unipolar large-scale field, which at first sight could indicate that it is not likely related to the preexisting gigantic prominence. However, because the small-scale fields are not recovered with the ZDI technique, it is possible that polarity inversions caused by, e.g., bipolar regions could take place within the polar spot. Therefore, if the giant prominence originated within the polar spot region, where the stellar coronal field is open, the prominence could erupt without suppression by the closed dipolar magnetic fields (see, e.g., K. M. Strickert et al. 2024). Furthermore, although subtle, it appears that the edge of the polar spot is in contact with the PIL, which might be related to the preexisting polar prominence. Future studies should include numerical simulations based on these magnetic field maps to validate each scenario.

In the above context, the assumption of a preexisting prominence or filament along the PIL suggests that, following its eruption, postflare dimming or enhancement should be anticipated at the center of the Hα line. The absence of clear evidence for this phenomenon may imply either the absence or minimal size of the preexisting prominence or filament. The effect may be relatively minor (T. Otsu et al. 2022), and it could be simply challenging to detect unambiguously. However, if a preexisting prominence or filament is located at low- to midlatitudes, the associated effects will be detected shifted by the rotational velocity. Looking at this Doppler effect is challenging at a spectral resolution of $R \sim 2000$; however, future high-dispersion spectroscopy may potentially allow for the localization of such preflare features.

4.3. Time Evolution of the Erupted Prominence: Can a CME Occur?

Here, we examine the temporal evolution of prominence eruptions based on the simplified models presented in Sections 3.2 and 3.3 and explore whether and how the eruption ultimately led to a stellar CME.

First, as shown in Figure 10 and described in Section 3.2, the 1D freefall model provides insights into the temporal variations in velocity and height of the prominence, with results derived from two distinct fittings to the Hα line data. These analyses suggest that the prominence's center of mass was lifted to between 0.5 and 1 stellar radii over a period of 40 minutes to 1 hr before it eventually fell back to the star. Moreover, in Section 3.3, a 1D hydrodynamic simulation of the flow along the expanding magnetic loop (pseudo 2D MHD model), without any radiative transfer model, also yields solutions that slightly indicate redshift at the end. A key issue observed is that this particular prominence eruption ultimately disappeared near zero velocity without exhibiting any redshift in the Hα line. We found that the anticipated timing for the onset of detectable redshift, about 1 hr after the event, coincides with the Hα line flux approaching near zero. This suggests a plausible scenario where the prominence, having possibly become too tenuous or heated (e.g., D. Seki et al. 2021 explain the solar cases), was no longer visible in the Hα line at the onset of detectable redshift.

Both models presented in Sections 3.2 and 3.3 support the scenario in which the prominences erupt near the limb and project at a certain angle in the vertical direction, predominantly in the direction of the Earth. Such tilted trajectories of prominence eruptions are commonly observed on the Sun (e.g., D. Seki et al. 2019), and thus, there is no contradiction in these findings. This tilt can be related to the surrounding magnetic environment and/or an uneven distribution of prominences within magnetic loops (see Figure 11). There is a possibility that strong magnetic fields or large-scale magnetic fields (such as strong toroidal magnetic fields) of EK Dra may be involved (see Figure 3), so verification by future 3D ejection models will be necessary. We emphasize that the obtained evolution likely represents one of the most well-characterized events in the study of stellar prominence eruptions across G/K/M-type stars.

As discussed in Paper I, it has been suggested that this prominence eruption could have evolved into a CME for various reasons: (i) The blueshift velocity slightly exceeded the escape velocity. (ii) Extrapolating from the relationship between the velocities of solar prominences and CMEs, the outer-layer coronal velocity is expected to exceed the escape velocity by enough. (iii) The criteria for the occurrence of a CME, based on the relationship between the length scale and velocity of solar prominence eruptions, were significantly surpassed. In this Paper II, the results from Sections 3.2 and 3.3 imply that the center of mass of the prominence might have fallen back toward the stellar surface. However, this only reflects the motion of the center of mass. Typically, prominences, like those on the Sun, are spatially extensive, and considering sufficient velocity dispersion, parts of these structures are expected to exceed the escape velocity, potentially leading to a CME. Indeed, the extended area for our eruptive prominence was estimated in Paper I (the large area was also inferred for prominences on a young solar-type star, V530 Persei; T. Q. Cang et al. 2020). Furthermore, 1D HD calculations based on solar physics in Section 3.3 support the scenario where, even if the prominence is falling, the magnetic loops continue to expand beyond the escape velocity. This substantiates the assertions made in Paper I, significantly reinforcing this model.

Finally, we discuss the possible role of centrifugal force in the evolution of prominences. In rapidly rotating solar-type

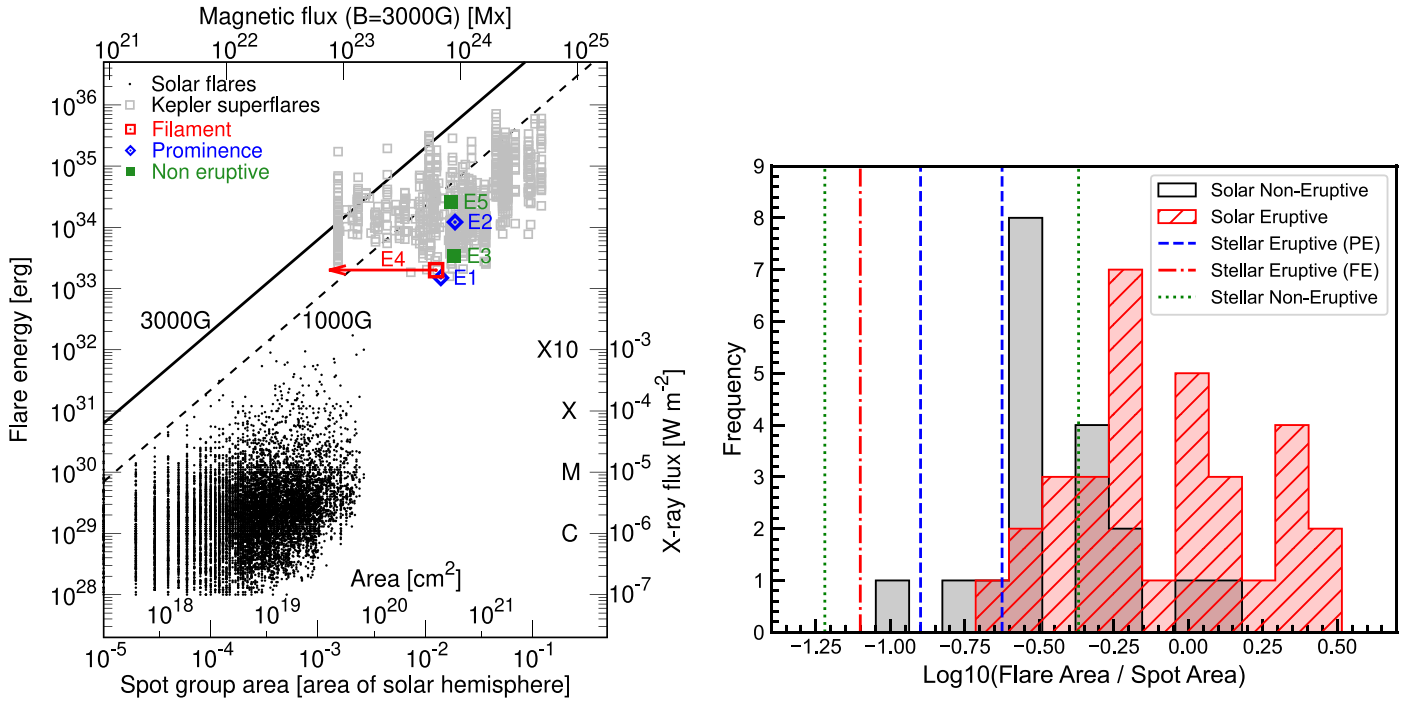

Figure 13. (a) The flare energy ($E_{\rm flare}$) as a function of spot group area ($A_{\rm spot}$) of solar flares and superflares on solar-type stars. The lower axis is the area of the spot group in the unit of the solar hemisphere ($1/2 \times A_\odot \sim 3 \times 10^{22}$ cm^2). The top horizontal axis is the magnetic flux of spots under the assumption of $B = 3000$ G. The left vertical axis shows the bolometric energy released by each flare. The right vertical axis GOES X-ray class where we assume that bolometric energies of 10^{29}, 10^{30}, 10^{31}, and 10^{32} erg scales to the GOES X-ray class of C, M, X, and X10, respectively. The black solid and dashed lines are the relationship between $E_{\rm flare}$ and $A_{\rm spot}$ for $B = 3000$ G and 1000 G, respectively. The relation assumes that the maximum flare energy against a given spot area can be explained by the total magnetic energy, i.e., $E_{\rm flare} = \frac{1}{8\pi} f B^2 A_{\rm spot}^{3/2}$, where f is a filling factor (e.g., K. Shibata et al. 2013). Here we did not add the error bars in the data because the xy-axis is in log scale, and the error range is too small to be plotted. (b) Comparison of the histograms for eruptive and non-eruptive events as a function of the ratio of flare area to spot area for the Sun and EK Dra. Stellar data are taken from Table 3. Solar data are taken from S. Toriumi et al. (2017), who derived the flare ribbon size from temporally stacked ultraviolet 1600 Å images. "FE" and "PE" mean filament and prominence eruptions, respectively.

stars with rotation periods of less than 1 day, prominences supported by centrifugal force due to the stellar rotation are often observed (referred to as "slingshot" prominences; A. Collier Cameron & R. D. Robinson 1989; J.-F. Donati et al. 2000; N. J. Dunstone et al. 2006; T. Q. Cang et al. 2020). Since EK Dra is a rapidly rotating star, though slower than stars having slingshot prominences, centrifugal force may aid in the ejection of prominences. The ratio of centrifugal force to gravity is given by $\omega^2(h + R_{\rm star})^3/GM_{\rm star}$, where h is the height above the stellar surface. This ratio is 0.01 at $h = 1R_{\rm star}$, 0.04 at $h = 2R_{\rm star}$, 0.33 at $h = 5R_{\rm star}$, and 1.1 at $h = 8R_{\rm star}$. Both models in Section 3 suggest that the prominence height from the stellar surface reaches about 0.5–1 stellar radius. This indicates that, within the framework and results of both eruption models, the contribution of centrifugal force is negligible, being only a few percent of the gravity. However, as mentioned earlier, some erupted prominences are expected to reach higher heights and could be significantly accelerated by centrifugal force, especially from around 8 stellar radii.

4.4. Relationship between Eruptive and Non-eruptive Superflares in Comparison with Starspot Area

Finally, we explore the relationship between spot size and flare magnitude by comparing solar flares to those observed on EK Dra. It is known that, for solar flares and CMEs, when the flare's length scale significantly exceeds the associated sunspot's length size, the flare tends to be eruptive rather than being suppressed by the magnetic field. Statistical analysis supports that larger flare length scales relative to sunspot length scales are more prone to result in CMEs (S. Toriumi et al. 2017; M. D. Kazachenko 2023). Given the scale-free nature of MHD, these may also apply to large stellar superflares.

Here, we propose the introduction of parameters transferred from solar research into the study of stellar eruptions: the flare energy relative to spot magnetic energy (Figure 13(a)) or the flaring area relative to spot area (Figure 13(b)). Figure 13(a) compares the flare energy-spot size relation between solar flares, flares on Kepler solar-type stars (S. Okamoto et al. 2021), and recent observations from EK Dra (Paper I). K. Shibata et al. (2013) proposed that the magnetic energy available within the spot determines the maximum flare magnitude, as in the lines in Figure 13, and flares close to this line can release a large portion of the stored free energy. We plotted events from EK Dra as either non-eruptive[30] or eruptive to investigate potential biases suggested in this graph. However, the limited sample of five cases shows no clear distinction. Given uncertainties such as which spot hosted each event or LOS ambiguities that might obscure observed

[30] Here, "non-eruptive" is defined as events where no blueshift was observed. However, considering LOS uncertainties, we cannot rule out that these were truly non-eruptive events only from this definition. If prominences erupt in a direction nearly perpendicular to the LOS, they will not be detected as blueshifts even if eruptions occur.

eruptions, a larger data set is necessary to discern trends. Nonetheless, the proximity of all EK Dra's events to the line in the graph suggests that a large portion of the magnetic energy in the spots was likely released for these superflares. Table 5 presents a comparison of the free magnetic energy,[31] flare radiation energy, and kinetic energy of prominence eruptions. Specifically, assuming a filling factor f of 0.1, the event E2 converts $23_{\pm 0.3}$% of the flare's magnetic energy into radiation energy, whereas the event E1 converts nearly all (170^{+370}_{-120}%) of the flare's magnetic energy into kinetic energy. These findings indicate that Events E1 and E2 represent extreme cases among the observed starspots.

Further, Figure 13(b) presents a histogram comparing the ratio of the flare length scale to the sunspot length scale for solar flares (data taken from S. Toriumi et al. 2017), with the eruptions from EK Dra overplotted. S. Toriumi et al. (2017) reported that this ratio statistically differs between eruptive and non-eruptive events for solar flares. Among EK Dra's events, we found that even smaller-scale flares relative to spot size were eruptive. Although the direct comparison with solar statistics by S. Toriumi et al. (2017) is not straightforward because they do not use the same flare size measurements, we plotted this as a reference, and we can at least say that overall both values are consistent. Although the current number of the sample is only five, this result may mean that the threshold may not necessarily hold for active stars or that eruptive events on active stars can emerge not from the dominant spots but possibly from clusters of smaller spots. The latter possibility is partly suggested by the fact that each spot size with TESS light-curve modeling ($(0.22–1.02) \times 10^{10}$ cm, as in Section 2.2) is smaller than that obtained by global TESS light curve (2.1×10^{10} cm, K. Namekata et al. 2024).

5. Summary and Conclusion

In Paper I, we reported the discovery of a gigantic prominence eruption on the young solar-type star, EK Dra. This prominence, occurring outside the stellar disk, is constrained by well-defined velocity variations over time, providing an excellent data set for investigating its dynamics. In the present paper, Paper II, our first objective is to estimate the dynamical evolution of this stellar prominence eruption. We employed a simple 1D freefall model (Section 3.2) and a 1D hydrodynamic simulation of the flow along the expanding magnetic loop (pseudo 2D MHD model; Section 3.3) to infer the direction of the ejection, changes in height, and the possible development of a magnetic loop. Furthermore, our second objective is to explore the origins of the prominence eruption and its relationship with the small-scale and large-scale magnetic field. For this purpose, we analyzed the TESS light curve (Section 2.2) and spectropolarimetric observation data obtained concurrently with the prominence observations (Section 2.1). These analyses allowed us to estimate the maps of starspots and the large-scale magnetic field and to examine their possible relationship with the prominence eruption. We suggest the following scenario for this event:

1. *Location*. The massive stellar prominence eruption is estimated to have originated approximately 12°–16° from the limb and was ejected at an angle of about 15°–24° relative to the line of sight (Section 3.2). This spatial evolution can be explained even by an expanding magnetic loop structure (Section 3.3, Figure 11).
2. *Evolution*. The center of mass of the prominence is expected to have reached its peak height about 40 minutes to 1 hr after an eruption, followed by an anticipated descent (Section 3.2, Figure 10). The timing coincides with the disappearance of the Hα line intensity. This can explain the puzzle in Paper I (see Section 1) by suggesting that the prominence may have disappeared at zero velocity merely because it became invisible in the Hα line. Our 1D hydrodynamic simulation of the flow along the expanding magnetic loop (pseudo 2D MHD model) indicates that even if the center of mass begins to fall, the loop itself continues to expand and can evolve into a CME (Section 4.3, Figure 11).
3. *Origin*. At the time of the prominence eruption, there were several large starspots at midlatitudes on the limb and a large starspot near the pole (Section 4.1, Figures 5, 3), consistent with the observed location of the base of the prominence eruption (Section 4.2). The large starspot at midlatitude, located on the PIL, is likely to be the source of the massive prominence, while we cannot rule out the possibility that the polar spot with a single polarity might be the source of the successful eruption.

There have been no studies that have extensively compared the direction of ejection and magnetic field environments based on observational data. Therefore, this is one of the most detailed studies in the field of stellar CME research, estimating the evolution and environmental context. These results inferred from the representative young Sun-like star provide valuable insights into the dynamic processes that likely influenced the environments of the early Earth, Mars, Venus, and young exoplanets.

To further investigate the correlation with spots, we conducted an analysis comparing the ratio of spot size to flare size, a criterion used on the Sun to differentiate between eruptive and non-eruptive events across all solar flares and the superflares observed on EK Dra. While the observed stellar flares likely released a significant amount of magnetic energy, any trends were not consistently evident. Given the current small sample size, it is expected that increasing the number of events in future studies may reveal some trends.

Finally, we summarize the future direction of this series of papers. Future work will focus intensively on comparing spots and active regions observed across multiple wavelengths. While the current study analyzed the configuration of spots at a snapshot, we will investigate the temporal changes in their global distribution and variations in active regions as observed in X-rays and Hα. Additionally, we plan to conduct more detailed dynamical modeling of stellar prominences in comparison with solar prominence observations and models and studies estimating the parameters of prominences through radiative transfer modeling. These efforts will allow us to analyze this event in greater detail.

[31] In Paper I, the free magnetic energy was mistakenly estimated under the f value of unity, although the text says that we assumed $f = 0.1$, which led to the incorrect conclusion that "Both the kinetic and radiation energies are much smaller than the stored magnetic energy of the active regions/starspots." Here we have recalculated the correct values and revised the discussion.

Acknowledgments

We would like to thank the referee for their valuable comments and suggestions, which have helped to improve the

quality of our manuscript. The authors thank Dr. Julián D. Alvarado-Gómez for fruitful comments on DI and ZDI maps. This work was supported by JSPS (Japan Society for the Promotion of Science) KAKENHI grant Nos. 21J00316 (K.N.), 24K17082 (K.I.), 20K04032, 20H05643, 24K00685 (H.M.), 21H01131 (H.M., K.I., and K.S.), 24H00248 (K.N., K.I., and H.M.), and 24K00680 (K.N., H.M., and K.S.). V.S.A. was supported by the GSFC Sellers Exoplanet Environments Collaboration (SEEC), which is funded by the NASA Planetary Science Division's Internal Scientist Funding Model, NASA NNH21ZDA001N-XRP F.3 Exoplanets Research Program grants and NICER Cycle 2 project funds and NICER DDT program. A.A.V. acknowledges funding from the European Research Council under the European Union's Horizon 2020 research and innovation program (grant agreement No. 817540, ASTROFLOW). Y.N. was supported by the NASA ADAP award program Number 80NSSC21K0632. P.H. acknowledges support from the grant 22-34841S of the Czech Science Foundation, and he was also supported by the program "Excellence Initiative–Research University" for the years 2020–2026 at the University of Wroclaw, project No. BPIDUB.4610.96.2021.KG. P.H. and J.W. were supported by the funding RVO:67985815. A.A.A. acknowledges Bulgarian NSF grant No. KP-06-N58/3 (2021). S.V.J. acknowledges the support of the DFG priority program SPP 1992 "Exploring the Diversity of Extrasolar Planets" (JE 701/+5-1). The spectroscopic data used in this paper were obtained through the program 22A-N-CN06 (PI: K.N.) with the 3.8 m Seimei telescope, which is located at Okayama Observatory of Kyoto University. This paper includes data collected with the TESS mission, obtained from the MAST data archive at the Space Telescope Science Institute (STScI). Funding for the TESS mission is provided by the NASA Explorer Program. STScI is operated by the Association of Universities for Research in Astronomy, Inc., under NASA contract NAS 5-26555. Some of the data presented in this paper were obtained from the Mikulski Archive for Space Telescopes (MAST) at the Space Telescope Science Institute. The specific observations analyzed can be accessed via doi:10.17909/xgds-j146. Numerical computations were carried out on Yukawa-21 at the Yukawa Institute for Theoretical Physics, Kyoto University. The authors acknowledge ideas from the participants in the workshop "Blazing Paths to Observing Stellar and Exoplanet Particle Environments" organized by the W.M. Keck Institute for Space Studies.

Facilities: Seimei, TBL, TESS.

Software: astropy (Astropy Collaboration et al. 2018), IRAF (D. Tody 1986), PyRAF (Science Software Branch at STScI 2012).

Appendix A
Initial Configurations and Parameters of the Pseudo 2D MHD Model

Figure 14 shows the initial configurations and parameters of a 1D hydrodynamic simulation of the flow along the expanding magnetic loop (pseudo 2D MHD model; Section 3.3) described in K. Ikuta & K. Shibata (2024) and K. Ikuta et al. (2024, in preparation). The parameter details are described in Section 3.3.

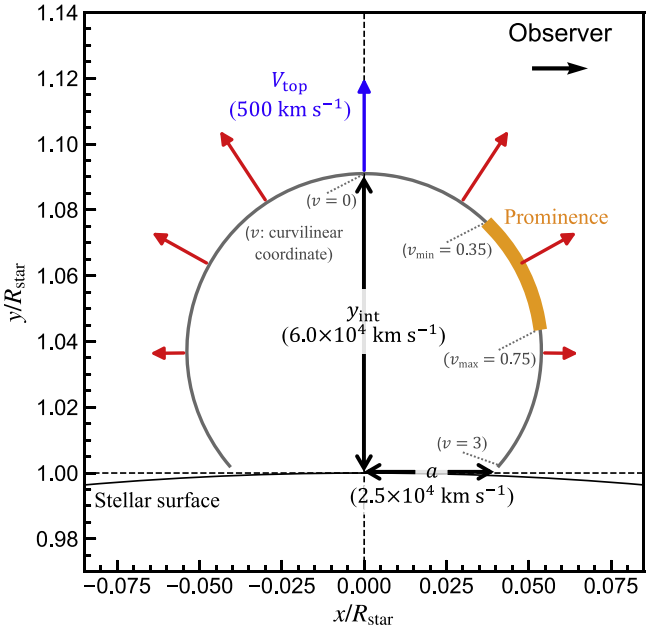

Figure 14. Initial configurations and parameters of a 1D hydrodynamic simulation of the flow along the expanding magnetic loop (pseudo 2D MHD model; Section 3.3) described in K. Ikuta & K. Shibata (2024) and K. Ikuta et al. (2024, in preparation). The initial position of the prominence is indicated by the thick orange line. In our model, specifying the velocity parameter at the loop apex, V_{top} (blue arrow), automatically determines the velocity distribution in the other parts of the magnetic loop (red arrows).

Appendix B
Spatial Resolution of (Zeeman) Doppler Imaging

Here we evaluate the spatial resolution of DI and ZDI maps. The spatial resolution of obtained DI and ZDI maps is given as $\delta l = 90^\circ \cdot \frac{\Delta\lambda}{\lambda}\frac{c}{v\sin i}$ or $360^\circ \cdot \Delta\phi$, where c is the light speed, $v \sin i$ is the stellar projected rotational velocity, and $\Delta\phi$ is the average observing phase coverage difference. Here, spectral resolution $\frac{\Delta\lambda}{\lambda}$ is $\sim$1/65,000, $v \sin i$ is 16.4 km s^{-1}, and $\Delta\phi$ is 1/16 (see Table 1). Therefore, the spatial resolution can be estimated as $\sim$25.°3 or $\sim$22.°5. However, the criterion presented here tends to underestimate the size of the smallest resolved element as it is limited by the resolving power of the spectrograph, while the width of the local line profile should also be the limiting factor for NARVAL.

ORCID iDs

Kosuke Namekata https://orcid.org/0000-0002-1297-9485
Kai Ikuta https://orcid.org/0000-0002-5978-057X
Pascal Petit https://orcid.org/0000-0001-7624-9222
Vladimir S. Airapetian https://orcid.org/0000-0003-4452-0588
Aline A. Vidotto https://orcid.org/0000-0001-5371-2675
Petr Heinzel https://orcid.org/0000-0002-5778-2600
Jiří Wollmann https://orcid.org/0000-0002-7618-9394
Hiroyuki Maehara https://orcid.org/0000-0003-0332-0811
Yuta Notsu https://orcid.org/0000-0002-0412-0849
Shun Inoue https://orcid.org/0000-0003-3085-304X
Stephen Marsden https://orcid.org/0000-0001-5522-8887
Julien Morin https://orcid.org/0000-0002-4996-6901
Sandra V. Jeffers https://orcid.org/0000-0003-2490-4779
Coralie Neiner https://orcid.org/0000-0003-1978-9809
Rishi R. Paudel https://orcid.org/0000-0002-8090-3570

Antoaneta A. Avramova-Boncheva https://orcid.org/0009-0001-5099-8070
Keith Gendreau https://orcid.org/0000-0001-7115-2819

References

Airapetian, V. S., Glocer, A., Gronoff, G., Hébrard, E., & Danchi, W. 2016, NatGe, 9, 452
Altschuler, M. D., Levine, R. H., Stix, M., & Harvey, J. 1977, SoPh, 51, 345
Alvarado-Gómez, J. D., Drake, J. J., Cohen, O., Moschou, S. P., & Garraffo, C. 2018, ApJ, 862, 93
Araki, T., & Ikeda, K. 2013, NN, 43, 33
Aschwanden, M. J. 2017, ApJ, 847, 27
Astropy Collaboration, Price-Whelan, A. M., Sipőcz, B. M., et al. 2018, AJ, 156, 123
Audard, M., Güdel, M., Drake, J. J., & Kashyap, V. L. 2000, ApJ, 541, 396
Audard, M., Güdel, M., & Guinan, E. F. 1999, ApJL, 513, L53
Ayres, T. R. 2015, AJ, 150, 7
Basri, G. 2018, ApJ, 865, 142
Benz, A. O. 2017, LRSP, 14, 2
Berdyugina, S. V., & Järvinen, S. P. 2005, AN, 326, 283
Cang, T. Q., Petit, P., Donati, J. F., et al. 2020, A&A, 643, A39
Claret, A., & Southworth, J. 2023, A&A, 674, A63
Cliver, E. W., Schrijver, C. J., Shibata, K., & Usoskin, I. G. 2022, LRSP, 19, 2
Collier Cameron, A., & Robinson, R. D. 1989, MNRAS, 236, 57
Colombo, S., Petralia, A., & Micela, G. 2022, A&A, 661, A148
Cranmer, S. R. 2017, ApJ, 840, 114
Crespo-Chacón, I., Montes, D., García-Alvarez, D., et al. 2006, A&A, 452, 987
Crosley, M. K., & Osten, R. A. 2018a, ApJ, 856, 39
Crosley, M. K., & Osten, R. A. 2018b, ApJ, 862, 113
Dere, K. P., Brueckner, G. E., Howard, R. A., et al. 1997, SoPh, 175, 601
DeRosa, M. L., Brun, A. S., & Hoeksema, J. T. 2012, ApJ, 757, 96
Donati, J.-F., Howarth, I. D., Jardine, M. M., et al. 2006, MNRAS, 370, 629
Donati, J.-F., Mengel, M., Carter, B. D., et al. 2000, MNRAS, 316, 699
Donati, J.-F., Semel, M., Carter, B. D., Rees, D. E., & Cameron, A. C. 1997, MNRAS, 291, 658
Dunstone, N. J., Barnes, J. R., Cameron, A. C., & Jardine, M. 2006, MNRAS, 365, 530
Eason, E. L. E., Giampapa, M. S., Radick, R. R., Worden, S. P., & Hege, E. K. 1992, AJ, 104, 1161
Emslie, A. G., Dennis, B. R., Shih, A. Y., et al. 2012, ApJ, 759, 71
Feinstein, A. D., Montet, B. T., Foreman-Mackey, D., et al. 2019, PASP, 131, 094502
Flores Soriano, M., & Strassmeier, K. G. 2017, A&A, 597, A101
Folsom, C. P., Bouvier, J., Petit, P., et al. 2018, MNRAS, 474, 4956
Folsom, C. P., Petit, P., Bouvier, J., et al. 2016, MNRAS, 457, 580
Foreman-Mackey, D., Hogg, D. W., Lang, D., & Goodman, J. 2013, PASP, 125, 306
Fuhrmeister, B., Czesla, S., Schmitt, J. H. M. M., et al. 2018, A&A, 615, A14
Fuhrmeister, B., Lalitha, S., Poppenhaeger, K., et al. 2011, A&A, 534, A133
Fuhrmeister, B., Liefke, C., Schmitt, J. H. M. M., & Reiners, A. 2008, A&A, 487, 293
Gibson, S. E., & Low, B. C. 1998, ApJ, 493, 460
Güdel, M. 2007, LRSP, 4, 3
Güdel, M., Guinan, E. F., & Skinner, S. L. 1997, ApJ, 483, 947
Gunn, A. G., Doyle, J. G., Mathioudakis, M., Houdebine, E. R., & Avgoloupis, S. 1994, A&A, 285, 489
Herbst, K., Papaioannou, A., Airapetian, V. S., & Atri, D. 2021, ApJ, 907, 89
Hirayama, T. 1986, NASCP, 2442, 149
Honda, S., Notsu, Y., Namekata, K., et al. 2018, PASJ, 70, 62
Houdebine, E. R., Foing, B. H., & Rodono, M. 1990, A&A, 238, 249
Hukushima, K., & Nemoto, K. 1996, JPSJ, 65, 1604
Ikuta, K., Maehara, H., Notsu, Y., et al. 2020, ApJ, 902, 73
Ikuta, K., Namekata, K., Notsu, Y., et al. 2023, ApJ, 948, 64
Ikuta, K., & Shibata, K. 2024, ApJ, 963, 50
Inoue, S., Enoto, T., Namekata, K., et al. 2024, PASJ, 76, 175
Inoue, S., Maehara, H., Notsu, Y., et al. 2023, ApJ, 948, 9
Jardine, M., Collier Cameron, A., & Donati, J.-F. 2002, MNRAS, 333, 339
Järvinen, S. P., Strassmeier, K. G., Carroll, T. A., Ilyin, I., & Weber, M. 2018, A&A, 620, A162
Jeffers, S. V., & Keller, C. U. 2009, in AIP Conf. Ser. 1094, 15th Cambridge Workshop on Cool Stars, Stellar Systems, and the Sun, ed. E. Stempels (Melville, NY: AIP), 664
Johnstone, C. P., Khodachenko, M. L., Lüftinger, T., et al. 2019, A&A, 624, L10
Kazachenko, M. D. 2023, ApJ, 958, 104
Kipping, D. M. 2012, MNRAS, 427, 2487
Kobayashi, K., Ise, J.-i., Aoki, R., et al. 2023, Life, 13, 1103
Kochukhov, O., Hackman, T., Lehtinen, J. J., & Wehrhahn, A. 2020, A&A, 635, A142
Kochukhov, O., Makaganiuk, V., & Piskunov, N. 2010, A&A, 524, A5
Koller, F., Leitzinger, M., Temmer, M., et al. 2021, A&A, 646, A34
Leitzinger, M., & Odert, P. 2022, SerAJ, 205, 1
Leitzinger, M., Odert, P., & Greimel, R. 2024, MNRAS, 532, 1486
Linsky, J. 2019, Host Stars and their Effects on Exoplanet Atmospheres: An Introductory Overview, Lecture Notes in Physics, Vol. 955 (Cham: Springer)
Linsky, J. L., Bushinsky, R., Ayres, T., Fontenla, J., & France, K. 2012, ApJ, 745, 25
Linsky, J. L., Fontenla, J., & France, K. 2014, ApJ, 780, 61
López Ariste, A., Georgiev, S., Mathias, P., et al. 2022, A&A, 661, A91
Low, B. C. 1984, ApJ, 281, 392
Loyd, R. O. P., Mason, J. P., Jin, M., et al. 2022, ApJ, 936, 170
Maehara, H., Notsu, Y., Namekata, K., et al. 2021, PASJ, 73, 44
Maehara, H., Shibayama, T., Notsu, S., et al. 2012, Natur, 485, 478
Metcalfe, T. S., Buzasi, D., Huber, D., et al. 2023, AJ, 166, 167
Miyake, F., Usoskin, I., & Poluianov, S. 2019, Extreme Solar Particle Storms; The Hostile Sun (Bristol: IOP Publishing)
Mohan, A., Mondal, S., Wedemeyer, S., & Gopalswamy, N. 2024, A&A, 686, A51
Muheki, P., Guenther, E. W., Mutabazi, T., & Jurua, E. 2020a, A&A, 637, A13
Muheki, P., Guenther, E. W., Mutabazi, T., & Jurua, E. 2020b, MNRAS, 499, 5047
Namekata, K., Airapetian, V. S., Petit, P., et al. 2024, ApJ, 961, 23
Namekata, K., Davenport, J. R. A., Morris, B. M., et al. 2020, ApJ, 891, 103
Namekata, K., Maehara, H., Honda, S., et al. 2022a, arXiv:2211.05506
Namekata, K., Maehara, H., Honda, S., et al. 2022b, ApJL, 926, L5
Namekata, K., Maehara, H., Honda, S., et al. 2022c, NatAs, 6, 241
Namekata, K., Maehara, H., Notsu, Y., et al. 2019, ApJ, 871, 187
Namekata, K., Toriumi, S., Airapetian, V. S., et al. 2023, ApJ, 945, 147
Notsu, Y., Kowalski, A. F., Maehara, H., et al. 2024, ApJ, 961, 189
Notsu, Y., Maehara, H., Honda, S., et al. 2019, ApJ, 876, 58
Okamoto, S., Notsu, Y., Maehara, H., et al. 2021, ApJ, 906, 72
Osten, R. A., & Wolk, S. J. 2015, ApJ, 809, 79
Osten, R. A., & Wolk, S. J. 2017, in IAU Symp. 328, Living Around Active Stars, ed. D. Nandy, A. Valio, & P. Petit (Cambridge: Cambridge Univ. Press), 243
Otsu, T., Asai, A., Ichimoto, K., Ishii, T. T., & Namekata, K. 2022, ApJ, 939, 98
Petit, P., Donati, J.-F., & Collier Cameron, A. 2002, MNRAS, 334, 374
Réville, V., Folsom, C. P., Strugarek, A., & Brun, A. S. 2016, ApJ, 832, 145
Ricker, G. R., Winn, J. N., Vanderspek, R., et al. 2015, JATIS, 1, 014003
Ryabchikova, T., Piskunov, N., Kurucz, R. L., et al. 2015, PhyS, 90, 054005
Scelsi, L., Maggio, A., Peres, G., & Pallavicini, R. 2005, A&A, 432, 671
Schrijver, C. J., & DeRosa, M. L. 2003, SoPh, 212, 165
Science Software Branch at STScI 2012, PyRAF: Python Alternative for IRAF, Astrophysics Source Code Library, ascl:1207.011
See, V., Jardine, M., Vidotto, A. A., et al. 2015, MNRAS, 453, 4301
Seki, D., Otsuji, K., Ishii, T., et al. 2019, SunGe, 14, 95
Seki, D., Otsuji, K., Ishii, T. T., Asai, A., & Ichimoto, K. 2021, EP&S, 73, 58
Semel, M. 1989, A&A, 225, 456
Şenavcı, H. V., Kılıçoğlu, T., Işık, E., et al. 2021, MNRAS, 502, 3343
Sharma, S. 2017, ARA&A, 55, 213
Shibata, K. 1980, SoPh, 66, 61
Shibata, K., Isobe, H., Hillier, A., et al. 2013, PASJ, 65, 49
Shibata, K., & Magara, T. 2011, LRSP, 8, 6
Shibayama, T., Maehara, H., Notsu, S., et al. 2013, ApJS, 209, 5
Strassmeier, K. G., & Rice, J. B. 1998, A&A, 330, 685
Strickert, K. M., Evensberget, D., & Vidotto, A. A. 2024, MNRAS, 533, 1156
Temmer, M. 2021, LRSP, 18, 4
Tody, D. 1986, Proc. SPIE, 627, 733
Toriumi, S., Schrijver, C. J., Harra, L. K., Hudson, H., & Nagashima, K. 2017, ApJ, 834, 56
Usoskin, I. G. 2023, LRSP, 20, 2
Veronig, A. M., Odert, P., Leitzinger, M., et al. 2021, NatAs, 5, 697
Vida, K., Kriskovics, L., Oláh, K., et al. 2016, A&A, 590, A11
Vida, K., Leitzinger, M., Kriskovics, L., et al. 2019, A&A, 623, A49

Vidotto, A. A., Gregory, S. G., Jardine, M., et al. 2014, MNRAS, 441, 2361
Vidotto, A. A., Jardine, M., Morin, J., et al. 2013, A&A, 557, A67
Villadsen, J., & Hallinan, G. 2019, ApJ, 871, 214
Vogt, S. S., & Penrod, G. D. 1983, PASP, 95, 565
Waite, I. A., Marsden, S. C., Carter, B. D., et al. 2017, MNRAS, 465, 2076
Wood, B. E., Müller, H.-R., Redfield, S., et al. 2021, ApJ, 915, 37
Wood, B. E., Müller, H. R., Zank, G. P., Linsky, J. L., & Redfield, S. 2005, ApJL, 628, L143
Yamashita, M., Itoh, Y., & Oasa, Y. 2022, PASJ, 74, 1295
Zic, A., Murphy, T., Lynch, C., et al. 2020, ApJ, 905, 23